Journal of Alloys and Compounds 904 (2022) 163941

Contents lists available at ScienceDirect

Journal of Alloys and Compounds

journal homepage: www.elsevier.com/locate/jalcom

On the enhanced hardening ability and plasticity mechanisms in a novel Mn-added CoCrNi medium entropy alloy during high-pressure torsion

Kaushal Kishore[a,b], Avanish Kumar Chandan[a,c,*], Pham Tran Hung[d], Saurabh Kumar[e], Megumi Kawasaki[f], Jenő Gubicza[d,**]

[a] Academy of Scientific and Innovative Research (AcSIR), Ghaziabad 201002, India
[b] Research & Development and Scientific Services, Tata Steel Limited, Jamshedpur 831007, India
[c] Materials Engineering Division, National Metallurgical Laboratory CSIR, Jamshedpur 831007, India
[d] Department of Materials Physics, Eötvös Loránd University, P.O.B. 32, Budapest H-1518, Hungary
[e] Department of Metallurgical Engineering and Materials Science, Indian Institute of Technology, Bombay, Mumbai 400076, India
[f] School of Mechanical, Industrial and Manufacturing Engineering, Oregon State University, Corvallis, OR 97331, USA

ARTICLE INFO

Article history:
Received 16 November 2021
Received in revised form 7 January 2022
Accepted 21 January 2022
Available online 29 January 2022

Keywords:
High entropy alloy
High pressure torsion
Gradient microstructure
Twinning induced plasticity
Dislocation density
Nano-structure

ABSTRACT

Microstructure and texture evolution during high-pressure torsion (HPT) of a novel Mn-added CoCrNi medium entropy alloy ($Co_{33}Ni_{33}Cr_{19}Mn_{15}$) is investigated for the first time. The alloy exhibited a rapid rise in hardness at relatively low shear strains ($\gamma \leq 20$). It is attributed to an extensive dislocation activity to achieve saturation in dislocation density of ~10^{16} m^{-2}, combined TWIP and TRIP effects and microstructural refinement. At higher shear strain, hardness increased at much reduced rates owing to saturation of dislocation density, twin fault probability and the TRIP effect, besides continued grain refinement for severe nano-structuring led to subsequent strengthening. The FCC phase showed remarkable stability except a small degree of initial deformation-induced HCP martensitic transformation in an early stage of HPT. The ideal shear texture components were observed at low shear strain, and these continued to evolve up to 5 turns of HPT processing. For similar HPT processing conditions, the studied alloy showed superior hardness (~650 Hv) compared to a wide spectrum of FCC materials, which is ascribed to a combination of the strengthening mechanisms of Taylor hardening, the TRIP and TWIP effects and Hall-Petch strengthening resulting from the nano-structured grains having an average size of ~35 nm.

1. Introduction

The introduction of multi-principal element alloys (MPEAs) has widened the compositional space for alloy design many-folds compared to conventional alloys consisting of only one principal element [1–3]. In early 2004, an initial class of MPEAs with 5 or more principal elements in an equiatomic ratio having entropy of mixing > 1.5 R was termed to be "high entropy alloys (HEAs)" [4,5]. The observed single-phase structure in such alloys was attributed to an entropy-driven reduction in the free energy helping in phase stability. However, many recent studies suggested that these HEAs are often metastable and are prone to deformation and/or thermally-induced phase transformations [6–10]. In quest of improving mechanical and functional properties, researchers have started to investigate the alloys with non-equiatomic compositions, such as $Al_9(CoCrFeMnNi)_{91}$ [11], $FeCoNiCrTi_{0.2}$ [12], various non-equiatomic FeMnCoCrNi alloys [13], $Fe_{40}Mn_{40}Co_{10}Cr_{10}$ [14] etc. Indeed, with a deviation from the classical definition of HEA, the alloys having non-equiatomic compositions with suitable processing routes have demonstrated an excellent combination of strength and ductility [15] and additional superior properties for a wide range of applications [16–20]. For instance, Wang et al. showed that a bulk as-cast $AlCr_{1.3}TiNi_2$ eutectic high entropy alloy (EHEA) has superior strength at both room and high temperatures in comparison with some well-known Ni and Ti based alloys [16]. Furthermore, a deviation from the exact eutectic composition of EHEAs does not alter the castability, the strength and the ductility significantly over a wide range of temperature, and this finding is beneficial for the large-scale industrial production of EHEAs as well as their potential usage for cryogenic applications [17]. Likewise, a non-equiatomic CoCrCuNiAl

* Correspondence to: MTE Division, CSIR-NML, P.O.: Burmamines, Jamshedpur 831007, Jharkhand, India.
** Corresponding author.
E-mail addresses: avanish@nmlindia.org (A.K. Chandan), jeno.gubicza@ttk.elte.hu (J. Gubicza).

https://doi.org/10.1016/j.jallcom.2022.163941
0925-8388/

HEA was used for cladding and exhibited good bonding with the substrate along with low dilution and higher micro-hardness compared to conventional FCC alloys [18]. Recently, Liang et al. showed a successful application of valence electron concentration and a new PHACOMP method for designing corrosion resistant CrCoFeMoNi HEAs [19]. They found that the non-equimolar CrCoFeMoNi HEAs with a single FCC phase without precipitates can have comparable corrosion resistance with Hastelloy C276. Similarly, a non-equiatomic $Ti_2ZrHfV_{0.5}Mo_{0.2}$ HEA exhibited an exceptional resistance against helium ion irradiation compared to conventional alloys [20].

Although HEAs with non-equiatomic compositions can achieve exceptional properties, further improvements are possible by applying suitable processing routes for microstructural refinement. Conventional thermomechanical processes have a limitation in obtaining microstructure with micron length scale grains and therefore many exotic structural and functional properties which are possible with nano-structured grains are seldom achieved. To this end, the severe plastic deformation techniques such as equal-channel angular pressing (ECAP), accumulative roll bonding (ARB), friction stir processing (FSP), high-pressure torsion (HPT) etc. are well established for achieving extensive microstructural refinement and the associated improvements in the properties [21–23].

HEAs with a face-centered cubic (FCC) crystal structure have attracted significant attention for their superior mechanical properties owing to their large strain hardening ability resulting from the presence of adequate slip systems and the possibility of transformation induced plasticity (TRIP) and/or twinning induced plasticity (TWIP) effects [24–26]. The micro-mechanism of deformation in FCC materials is strongly governed by the stacking fault energy (SFE) [27]. Although, there is a reasonably good understanding of the predominant mechanism(s) of plastic deformation in FCC metals and alloys during conventional modes of loading such as uniaxial tensile or compression states [28–30], it is debatable for severe plastic deformation by HPT processing owing to its involvement of very high pressure, large shear strains and the intense microstructural refinement to ultrafine grains or nanostructure [31–33]. Recently, Sathiyamoorthi et al. and Chandan et al. studied the microstructure evolution during HPT in a non-equiatomic $Fe_{40}Mn_{40}Co_{10}Cr_{10}$ TWIP HEA [34,35] for which the SFE at room temperature was reported to be 37.7 mJ/m^2 [36]. In line with the conventional relationship between SFE and deformation behaviour, the occurrence of dislocation slip and twinning was shown in this TWIP HEA during room temperature tensile deformation owing to the medium SFE [36]. Moreover, these studies observed the occurrence of extensive FCC-to-HCP transformation during HPT processing [34,35]. Furthermore, HPT processing induced nano-scale chemical inhomogeneity in a $(FeNiCoCu)_{1-x}Ti_xAl_x$ HEA, which is unlikely to occur during conventional thermo-mechanical processing [37]. Recently, Edalati et al. studied the deformation behavior of an AlFeCoNiCu dual-phase HEA during HPT and reported different mechanisms of deformation in the FCC and BCC phases [38]. It was observed that the FCC phase deformed by the formation of twins and stacking faults, whereas the BCC phase deformed via dislocation glide leading to high accumulation of dislocations. By these accounts, it is evident that HPT processing can alter the microstructure evolution of HEAs in an unexpected manner and hence there is a scientific need to study the microstructural and mechanical responses of HEAs after HPT processing.

In terms of efficacy of HPT processing for materials, the extent of grain refinement and the achieved hardness are the two important measures [22]. An earlier study showed that for an equiatomic CoCrFeMnNi Cantor alloy processed under 6 GPa pressure for 5 turns of HPT the hardness increased to ~455 Hv [39]. A deviation from this composition has resulted in an enhanced hardness after HPT processing. For instance, under the similar processing condition, $(FeNiCoCu)_{86}Ti_7Al_7$ showed the hardness value of ~525 Hv [37]. Moreover, a further enhancement in hardness to ~610 Hv was achieved for a CoCrNi medium entropy alloy (MEA) under the similar HPT processing condition [40]. In terms of microstructural refinement, an average grain size of < 50 nm has been reported for the CoCrNi alloy, while a reasonably small grain size of tens of nanometers has been shown for the CoCrNiFeMn Cantor alloy after similar processing [39,40]. Recently, Chandan et al. highlighted a crucial role of Ni addition in altering the deformation mechanisms from predominant slip to TRIP and the extent of nano-structuring in non-equiatomic FeMnCoCr HEA processed by HPT [41]. These studies showing differences in hardness and the extent of nano-structuring highlight the significance of alloy chemistry in the evolution of the microstructure during HPT processing. As manganese is one of the vital elements in altering the SFE, the deformation mechanisms and therefore, strengthening mechanisms in Fe-rich alloys [42,43], we have fabricated a modified version of equiatomic CoCrNi alloy by partially replacing Cr by Mn to achieve a nominal composition of $Co_{33}Ni_{33}Cr_{19}Mn_{15}$ (at%) and studied its HPT response in detail. From our preliminary results using ThermoCalc software, Fig. 1 shows the role of replacement of Cr by Mn in the well-studied CoCrNi medium entropy alloy. Addition of Mn resulted in an increase in the free energy change due to FCC-to-HCP phase transformation ($\Delta G^{\gamma\rightarrow\varepsilon}$) towards a more positive value, thereby indicating the stabilization of a single-phase FCC structure. Further, as SFE is directly proportional to the free energy change, the modified alloy composition is expected to have an enhanced SFE compared to the CoCrNi alloy.

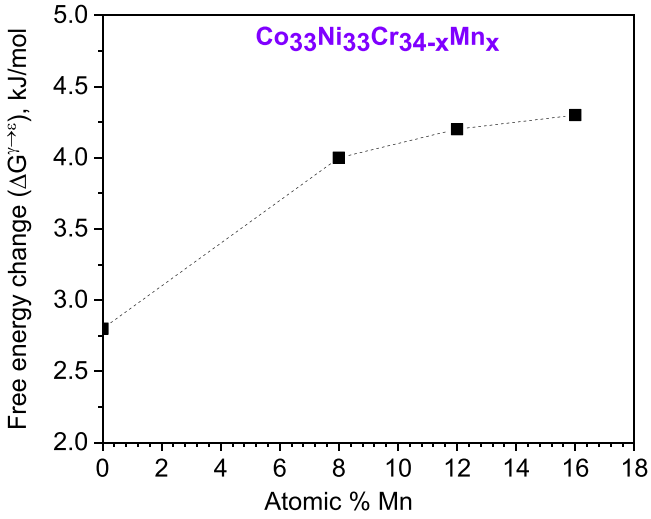

Fig. 1. Effect of a partial replacement of Cr by Mn on the free energy change $\Delta G^{\gamma\rightarrow\varepsilon}$ for CoCrNi alloy.

As HPT processing induces a gradient microstructure from the sample center to periphery, in this paper, the evolution of microstructure and hardness is studied as a function of the examined locations and the number of HPT turns. We also present the evolution of texture during HPT processing, as crystallographic texture can shed insights into the plastic deformation mechanisms and can also significantly influence the post-processing properties such as formability, strength-ductility trade-off, corrosion resistance and magnetic behaviour.

2. Experimental procedure

2.1. Processing of the samples

A vacuum induction melting route was used to produce a medium entropy alloy (MEA) with nominal composition of $Co_{33}Ni_{33}Cr_{19}Mn_{15}$ (at%). Each constituent element in the initial raw material had a purity of at least 99.9%. The actual composition of the studied MEA determined by X-ray fluorescence spectroscopy and

Table 1
Chemical composition of the studied alloy.

Elements	Co	Cr	Ni	Mn	Fe
Atomic %	33.13	19.04	32.87	14.91	0.05

validated using bulk energy dispersive X-ray spectroscopy is shown in Table 1.

A cast ingot of the alloy with dimension $50 \times 50 \times 70\ mm^3$ was subjected to homogenization heat treatment at 1200 °C for 1.5 h followed by sectioning to dimension $25 \times 50 \times 70\ mm^3$. Hot forging was conducted at ~1100 °C to obtain a plate with the thickness of 12.0 mm. Thereafter, hot rolling was carried out at a finished rolling temperature of 1000 °C to reduce the thickness to 6.0 mm. The thickness was further reduced to 2.0 mm via cold rolling operation. A solution annealing treatment at 900 °C for 25 min followed by water quenching was applied to the cold rolled sheet. A set of disc samples having a diameter of 10.0 mm and a thickness of 0.9 mm were machined for HPT processing. These discs surfaces were prepared using a silicon carbide emery paper with a grit size of 600 to obtain a similar surface roughness to avoid any variation in friction between the disc material and the anvils during HPT processing.

A quasi-constrained set-up of HPT processing was employed, whose details can be found in earlier works [35,44]. The schematic of the process is shown in Fig. 2(a-b). The quasi-constrained set-up allows a small flow of the material out between the upper and the lower anvils during processing, which results in a back-pressure, thereby minimizing the probability of slippage between the sample and the anvils. In the present work, 6 GPa pressure and 1 rpm rotation speed were used as HPT processing parameters for all the samples. The disc samples were subjected to ½, 1, 2 and 5 rotational turns at room temperature. It is established that the strain during HPT processing varies both as a function of the distance from the disc center as well as on the number of turns. Assuming pure torsion, shear strain, γ, during HPT processing can be expressed as [45]:

$$\gamma = \frac{2\pi rn}{t} \quad (1)$$

where r is the distance from the center of the disc, t is the thickness of the HPT-processed specimen and n is the number of rotations. Eq. (1) is subsequently used to evaluate the variation of micro-hardness within the specimens as a function of shear strain.

2.2. Study of the microstructure

The locations of the microstructural investigations on the HPT-processed discs are shown in Fig. 2(c). All microstructural investigations were carried out on the plane of the HPT-processed discs, near the surface. Microstructure observations were conducted at the centers and a distance of 4 mm from the center (referred as edge from here onwards) of the HPT discs. The disc samples were polished using different grits of silicon carbide emery papers starting from 120 to 2000. The sample surfaces were further polished using diamond pastes with 6, 3 and 1 µm sizes and were electropolished in a solution consisting of ethanol + perchloric acide with the ratio of 90:10 at −25 °C and 18 V. The microstructural investigations were conducted by X-ray diffraction (XRD) and transmission electron microscopy (TEM). These microstructural results were completed with bulk texture analysis using XRD at both disc center and edge locations. A monoclinic sample symmetry is used in the present study for texture analysis. Similar sample symmetry was used formerly for texture investigation in an HPT-processed FCC HEA [46].

XRD investigation of the initial material was carried out in the Bruker D8 Advance diffractometer. CuKα radiation was employed and the measurements were performed in Bragg–Brentano geometry over the angular range from 40° to 102° with a step size of 0.02° and a time per step of 2 s. The texture measurements for the samples after HPT processing were performed by a PANalytical Empyrean X-ray diffractometer. The spot size used for texture analysis was controlled by an opening of the incident beam aperture (width: 1 mm and height: 1 mm) and in the present case, the illuminated area was ~2.18 mm^2 at both disc center and edge locations. The XRD measurements were performed at the centers and edges of the HPT-processed discs by employing a Smartlab diffractometer (manufacturer: Rigaku, Japan) in θ-θ geometry with parallel beam and CuKα_1 radiation. The 2θ angle range for the XRD measurements was 35–105° for all specimens. A beam with the following dimension was utilized: length = 2 mm and width = 0.25 mm. A procedure of convolutional multiple whole profile (CMWP) fitting was used to perform X-ray diffraction line profile analysis (XLPA) in order to discern the values of various microstructural parameters such as crystallite (or diffraction domain) size, dislocation density, twin fault probability etc. which evolve during HPT processing. This method involves the fitting of the diffraction pattern by the sum of a background spline and the theoretical peak profiles. The theoretical peak

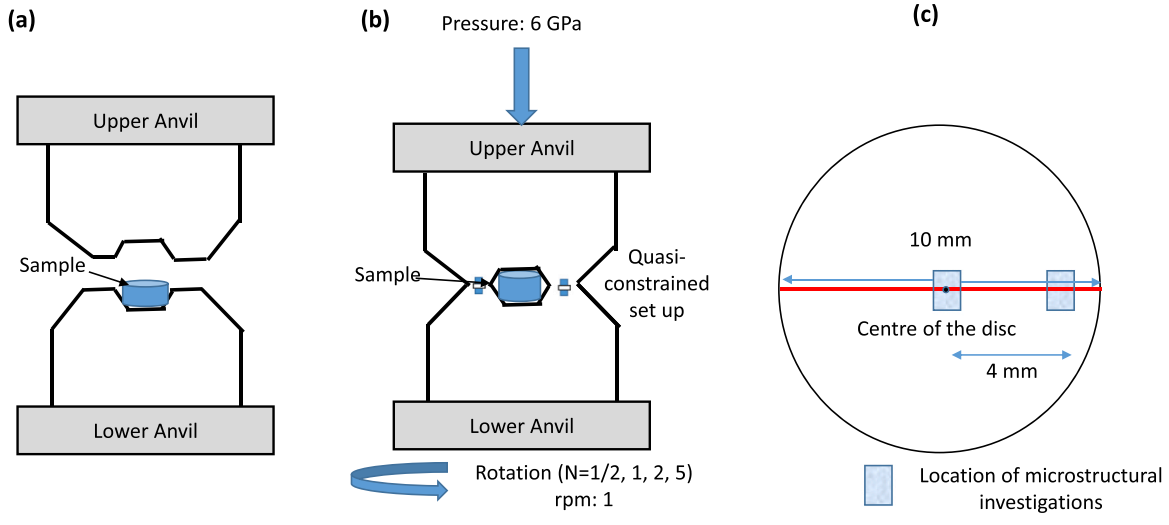

Fig. 2. Schematic representation of the quasi-constrained high pressure torsion (HPT) processing set-up and the characterization locations within a disc sample: (a) after placing a disc sample on the lower anvil, (b) the sample between the anvils during the processing, and (c) schematic showing the locations of microstructural investigations in the disc specimen (Red line shows a representative diameter of the HPT-processed disc where the hardness measurements were performed).

profiles are attained as the convolution of the calculated line profiles (which are related to crystallite size, dislocations and twin faults) and the instrumental peak. Since the massive plastic deformation during HPT processing resulted in a much higher peak broadening than the instrumental effect, the present study did not involve instrumental correction. The CMWP fitting yielded the dislocation density (ρ) and the area-weighted mean crystallite size ($< x >_{area}$) where the later quantity was deduced from the log-normal variance of the crystallite size distribution (σ^2) and the median (m) as $< x >_{area} = m \cdot exp(2.5\sigma^2)$. In addition, the twin fault probability (β) was also obtained by CMWP fitting. The quantity gives the fraction of {111} planes containing twin faults. A more detailed description of the CMWP fitting method can be found elsewhere [47].

For TEM investigations, first the HPT-processed samples were thinned down to 0.05–0.06 mm by mechanical polishing. Then, the samples were further thinned by employing a Gatan's dimple grinder followed by ion milling using a Gatan's PIPS II equipment to make the specimen electron transparent. It should be noted that a number of precautions were applied to prevent the formation of any artefact during the TEM sample preparation. For instance, a cold sample stage was used during ion milling. In addition, low energy milling was employed to avoid the formation of amorphous regions. Post-milling plasma cleaning was used to remove the sputtered particles from the surfaces of the TEM samples. JEOL's 200 kV JEM 2200FS was employed for the TEM and scanning transmission electron microscopy (STEM) investigations of the HPT-processed samples. The same facility was used for energy dispersive X-ray spectroscopy (EDS) examinations to obtain elemental maps for the HPT-processed specimens. The as-received specimen (prior to HPT processing) was characterized using XRD, scanning electron microscope (SEM)-EDS and electron backscattered diffraction (EBSD). EBSD and EDS detectors were attached to a FEI Nova Nano-SEM 430 equipment.

2.3. Hardness testing

A Vickers hardness tester (EMCO) was used for the hardness measurements under a load of 500 g with a dwell time of 30 s. At least five measurements were performed to compute an average hardness value and standard deviation for each selected examination location.

3. Results

3.1. Characterization of material prior to HPT processing

An X-ray diffractogram of the unprocessed specimen is shown in Fig. 3(a). The peak positions describe the structure of an FCC phase. No second phase was present, thereby confirming that the alloy in the initial state had a single-phase FCC structure. An inverse pole figure (IPF) map taken on the disc surface gives indexing with respect to FCC phase as shown in Fig. 3(b). The microstructure revealed the presence of polygonal grains with broad annealing twins as depicted in Fig. 3(b-c). An average grain size was measured to be 34 ± 8 µm (excluding annealing twins). In order to ascertain the chemical homogeneity of the alloy before HPT processing, elemental mapping using energy dispersive X-ray spectroscopy (EDS) of the constituent elements is shown in Fig. 3(d-g). Evidently, the distribution of the constituent elements in the alloy before nanostructuring is homogenous without any segregation. The texture in the rolling plane of the as-received sample was depicted using $\phi_2 = 0°$ and $\phi_2 = 45°$ ODF sections as presented in Fig. 3(h). This analysis indicates the presence of Goss, Brass and Copper texture components.

3.2. Phase evolution during HPT processing

FCC-to-HCP phase transformation (TRIP effect) is one of the possible strain accommodation mechanisms in FCC materials with low stacking fault energy [48]. Furthermore, HEAs with medium SFE can also undergo extensive deformation-induced phase transformation under HPT processing owing to very high pressure and large strains [35,49]. Fig. 4 shows the XRD plots obtained at the center and edge locations of the specimens subjected to different numbers of turns by HPT processing. In all cases, diffraction occurred from (111), (200), (220), (311) and (222) planes corresponds to an FCC crystal structure. This indicates an absence of predominant TRIP effect in this HEA despite severe straining by HPT processing up to 5 turns. Hence, the predominant mechanism of deformation can be slip of dislocations or twinning, which is investigated subsequently.

3.3. Dislocation density and substructure evolution during HPT

A detailed study on the XRD plots for the HPT-processed samples revealed important findings. Deformation-induced phase transformation was not observed, while the extensive peak broadening suggested an increase of micro-strain and/or a reduction in crystallite size in the HPT-processed specimens (Fig. 5). In practice, the full width at half maximum (FWHM) of the XRD peaks taken near the disc edge was significantly higher compared to the disc center for ½ turn, indicating a difference in the micro-strain and/or the crystallite size as shown in Fig. 5(a). Thus, the result implies greater micro-strain and/or finer crystallite size at the disc edge than in the center. It is interesting to note that in comparison with the ½ turn specimen a significant increase in broadening was observed at the center of the 1 turn specimen as depicted in Fig. 5(b), while the width of the peak did not increase at the edge location. This resulted in a much lesser difference between the FWHM values for the edge and center locations after 1 turn. On further increasing numbers of turns to 2 as shown in Fig. 5(c), the difference between the FWHM values at the center and edge locations vanished and similar peak breadths were maintained in the specimen through 5 turns as shown in Fig. 5(d). The overlapping peaks indicate a marked reduction in microstrain gradient and/or saturation of crystallite size between the disc centers and edges after high numbers of HPT turns.

It is worth noting that significant broadening was observed even in the center of the disc, where theoretically there should be zero shear strain (Eq. 1). Such an apparent paradox of significant accumulation of defects at the center of the HPT-processed disc can be resolved based on the findings of Estrin et al. [50]. They showed that both the first and second order strain gradient models, coupling the evolution of statistically stored dislocation and geometrically necessary dislocation densities can be successfully applied to HPT processing, so that the strain gradient progressively decreases from center to periphery of the discs with increasing numbers of HPT turns. Furthermore, it can also be understood by the fact that the non-zero strain in the adjacent locations can eventually impose strain at the center of the disc to maintain the continuity of the material. Moreover, introduction of non-zero strain at the center of HPT discs can also be attributed to an inevitable minor misalignment of the anvils as shown by Huang et al. [51,52]. Nonetheless, the spot size of 2 mm of the X-ray beam means that the signals are recorded not only from the center but from its vicinity as well where the area experiences non-zero shear strain based on Eq. (1). In this context, similar peak broadening near the disc center and edge is still an important indication of the marked mobility of dislocations and defect generation at both the locations and points towards the minimization of strain gradient with increasing numbers of HPT turns, which is in line with Estrin's strain gradient models [50].

Fig. 5(e) shows the Williamson-Hall plots for the as-received specimen and 2 turn HPT-processed specimen at its center and edge

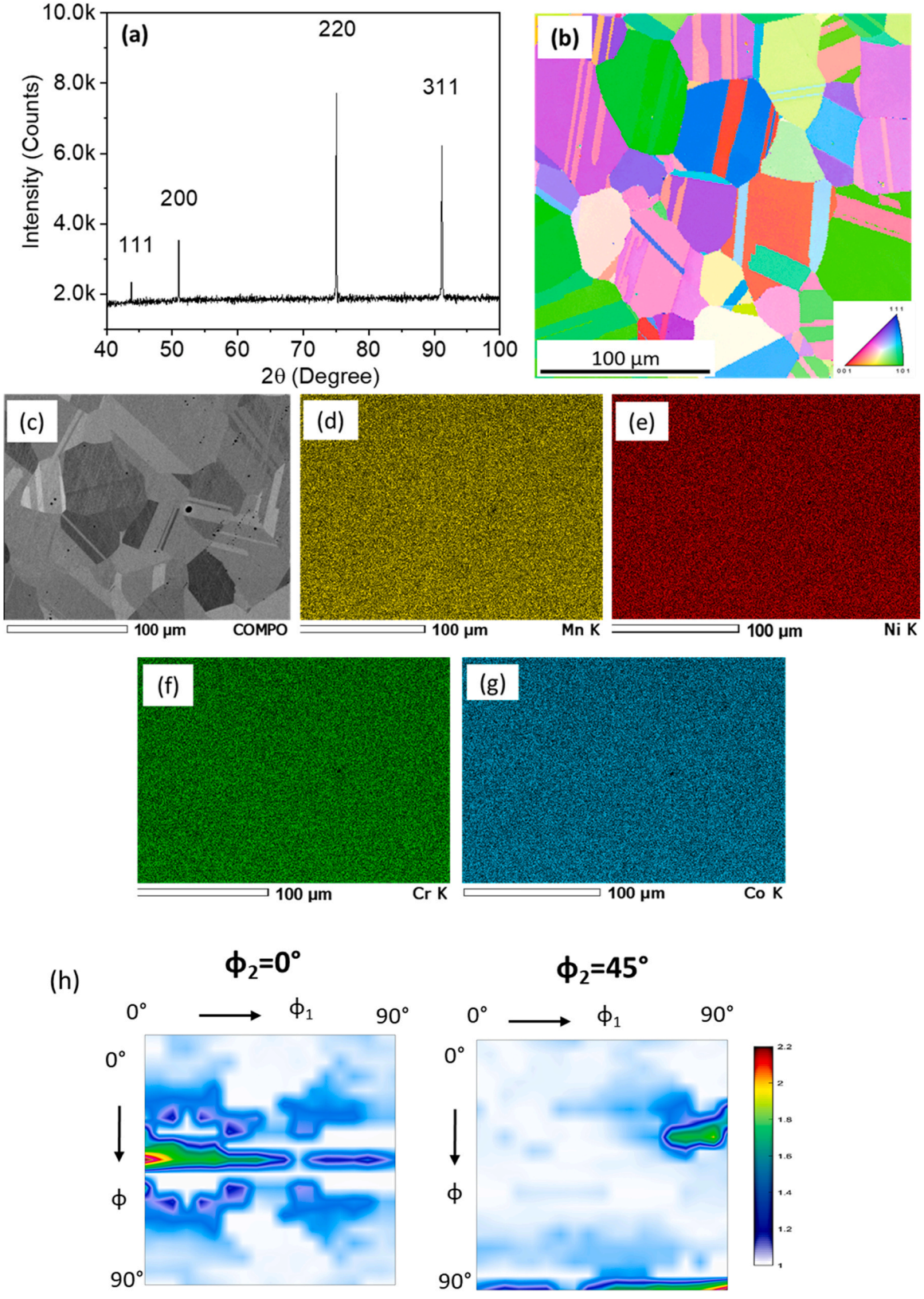

Fig. 3. Characterization of the specimen prior to HPT processing: (a) X-ray diffractogram, (b) Inverse Pole Figure (IPF) map, (c) Backscattered electron (BSE) micrograph, (d, e, f, g) elemental mapping of Mn, Ni Cr, and Co respectively, (h) bulk texture analysis in the rolling plane of the as-received sample depicted using $\phi_2 = 0°$ and $\phi_2 = 45°$ ODF sections.

locations. The peak broadening in the as-received specimen was very low and almost constant with increasing the magnitude of the diffraction vector (K). On the other hand, the peak broadening increased non-monotonically as a function of K for the 2 turns HPT-processed sample at both the edge and center locations. Similar non-monotonic trend in the peak broadening was observed for all the HPT-processed samples (not shown separately) which suggests dislocation-induced broadening of the XRD peaks. These observations

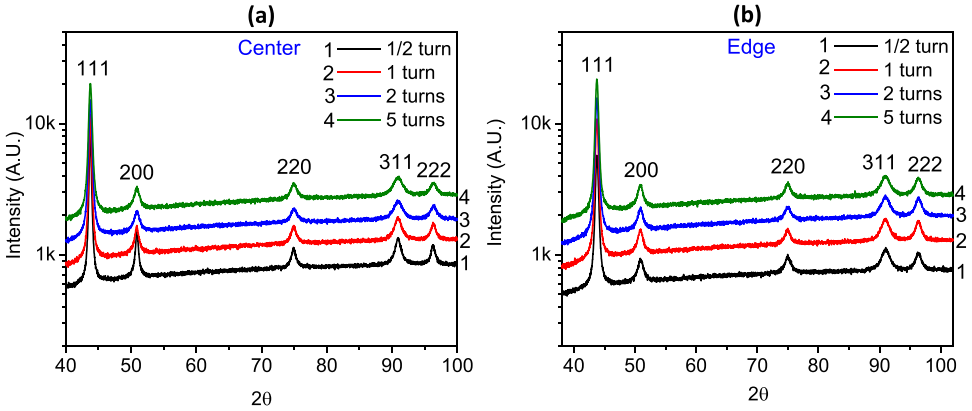

Fig. 4. X-ray diffraction patterns examined at (a) center and (b) edge of the HPT-processed disc specimens for different numbers of turns. The 2θ values are given in degrees in the horizontal axis.

indicate an absence of considerable amount of dislocations in the as-received sample whereas in the HPT-processed samples significant dislocation density must have been formed. XLPA employing CMWP fitting method was carried out to quantify the evolution of the microstructure such as the dislocation density, the crystallite size and the twin fault probability. An illustration of the CMWP fitting on an XRD pattern is presented in Fig. 5(f). The difference between the experimental and CMWP fitted diffractograms was near to zero for each two-theta value which indicated a good fitting.

Fig. 6 shows the evolution of the microstructural parameters determined by XLPA, namely, the dislocation density (ρ), the crystallite size ($< x >_{area}$) and the twin fault probability (β) as a function of the number of turns and the examined location in the HPT-processed specimens. A very high dislocation density of ~8×10^{15} m^{-2} was observed even at the center of the specimen processed by ½ turn as shown in Fig. 6(a), indicating a rapid rate of generation and multiplication of dislocations at a relatively early stage of HPT processing. However, a two-fold higher dislocation density, i.e., ~1.6×10^{16} m^{-2}, was observed near the edge of this specimen highlighting a highly heterogenous deformation along the radial direction. With increasing numbers of HPT turns, the difference in the dislocation density between the edge and the center decreased, indicating the microstructural evolution towards homogeneity. Nonetheless, the dislocation density at the edges is always greater than that at the centers till 2 turns, but thereafter it became nearly equal at both locations for 5 turns. Likewise, as shown in Fig. 6(b), the crystallite size was finer at the edges compared to the centers up to 1 turn of HPT processing. For the sample processed by 2 turns, the crystallite size at the center and the edge became nearly equal, which indicates attainment of the minimum possible crystallite size within the disc homogeneously. This is consistent with the saturation of these microstructural parameters for relatively low numbers of HPT turns for CoCrFeNi HEA [53]. In addition to the dislocation density and the crystallite size, the twin fault probability was also evaluated for both center and edge parts of the HPT-processed specimens and is presented in Fig. 6(c).

Table 2 summarizes the microstructural parameters obtained using CMWP analysis. The saturation of the dislocation density and the crystallite size with increasing the number of HPT turns is evident from the table. In addition, CMWP analysis indicated that the contributions of the different mechanisms to deformation changed with increasing strain. For instance, a very low value of twin fault probability of 0.3 ± 0.1% was observed at the center of the specimen after ½ turn of HPT. However, near the edge of the same specimen, it was as high as 1.2 ± 0.2%. The difference in twin fault probability indicates a greater propensity for deformation twinning at the edge location where a higher torsional strain was imposed. Thus, similar to dislocation density and crystallite size, twin fault probability also showed a dependence on shear strain which changes with the number of HPT turns and the location of investigation. With increasing the number of turns from ½ to 5, the twin fault probability increased from ~0.3 to ~1.6% at the centers of the discs, while there was only a marginal increase from ~1.2 to ~1.7% at the edges. This again suggests that the mechanisms of deformation and their extent of activation varied from the center to the edge and also with increasing numbers of turns. The features and mechanisms tend to saturate at the edges faster than in the centers of the discs.

3.4. Hardness evolution during HPT

Variation of micro-hardness along the diameter of the disc as a function of the number of HPT turns is depicted in Fig. 7(a). Hardness of the disc in the as-received condition was measured to be 194 ± 3 Hv that is depicted by a dotted line in the plot. For the ½ turn processed specimen, a marked increase in hardness to 331 ± 2 Hv was observed at the center of the disc. This increase in hardness is corroborated in part by a very high dislocation density of ~8×10^{15} m^{-2}, and it indicates the center of the disc experienced substantial strain leading to Taylor hardening. Furthermore, relatively fine crystallite size would also have contributed to the strengthening/hardening at the center of the disc. Compared to the hardness increase of nearly 65% at the disc center after ½ turn by HPT, greater than two-fold increase in hardness was observed at the disc edge where a maximum hardness of 582 Hv was measured. This can be explained by the two-fold higher dislocation density and finer crystallite size in the edge region of the ½ turn specimen. A monotonic increase in hardness was observed from the center to the edge in all specimens. A symmetric hardness profile across the diameter of the discs with respect to the center indicates the consistent gradations radially in strain, associated work hardening and other strengthening mechanisms from the centers to the edges. At any given location of the discs, higher the number of turns, higher is the micro-hardness. The variation of hardness with shear strain is shown in Fig. 7(b). Initially, there is a large increase in hardness with increasing shear strain, thereafter the slope of the trend goes down at the later stages. It is interesting to note that despite saturation of dislocation density, crystallite size and twin fault probability between the center and the edge in the specimen after HPT for 5 turns as shown in Table 1, a significant difference in hardness of ~200 Hv was observed between the disc center and edge. This suggests the significance of another strengthening effect in addition to the contributions to hardening by dislocations and twin faults. Since no significant TRIP effect is

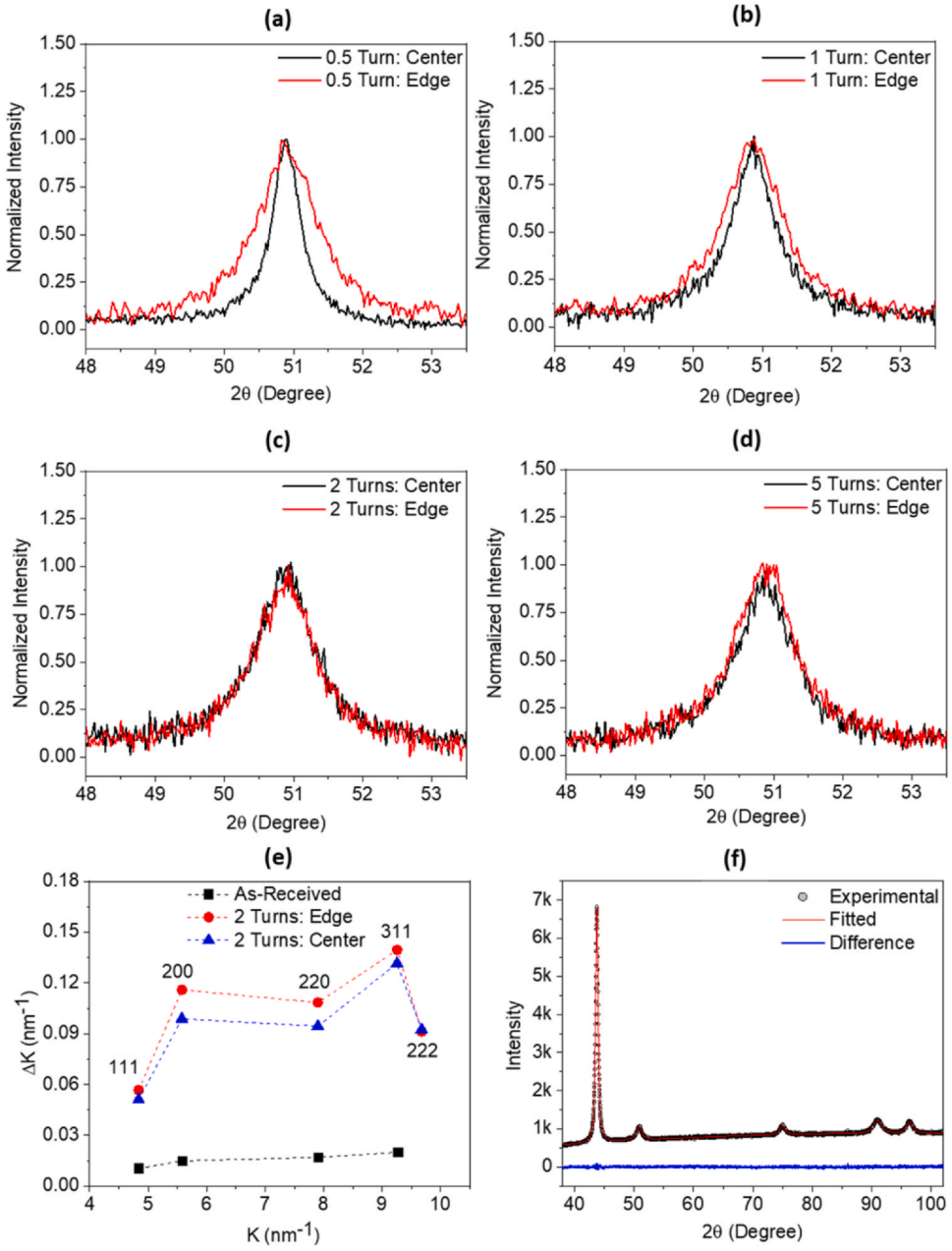

Fig. 5. Illustration of XRD peak broadening at center and edge for (200) peak: (a) ½ turn, (b) 1 turn (c) 2 turns, (d) 5 turns, (e)WH plot for the samples in as-received condition and at center and edge locations after 2 turns of HPT, (f) experimentally determined and fitted XRD pattern using CMWP method for 5 turns at edge location.

observed at any location based on XRD analysis, the possibility of additional strengthening by TRIP mechanism is precluded. It should be noted that the results of dislocation density, crystallite size and twin fault probability obtained by XLPA are characterized by considering much larger sample volume than that probed by hardness testing, where the length of the area examined by the X-ray beam was about 2 mm. Therefore, the hardness values averaged for 1 mm distances from the disc center should be compared with the microstructural parameters measured for the center by XLPA. In this regard, for 5 turns, this average hardness is ~465 Hv around center location (see Fig. 7(a)) which is still lower than ~640 Hv measured at 4 mm from the center (corresponding to the edge location studied by XLPA). To understand this difference in hardness, in-depth TEM and texture evolution investigations were carried out at the center and edge locations and is presented in the subsequent sections.

3.5. Microstructural investigation using transmission electron microscopy

Fig. 8(a) presents the bright field (BF) TEM micrograph at the center of the ½ turn HPT-processed specimen. High dislocation density is evident from dislocation forest even at such early stage of HPT processing. Furthermore, parallel and relatively coarse deformation bands with a spacing of ~110–180 nm were observed. The corresponding dark field (DF) micrograph is presented in the inset. A selected area diffraction (SAD) pattern in Fig. 8(b) taken at the field shown in Fig. 8(a) clearly indicates the formation of twins in the FCC phase after ½ turn. The SAD pattern was indexed w.r.t. the $[0\bar{1}1]$ and [101] zone axes corresponding to the FCC matrix (M) and twinned FCC phase (T), respectively. Additional deformation feature at the center of the ½ turn processed specimen is shown in Fig. 8(c)

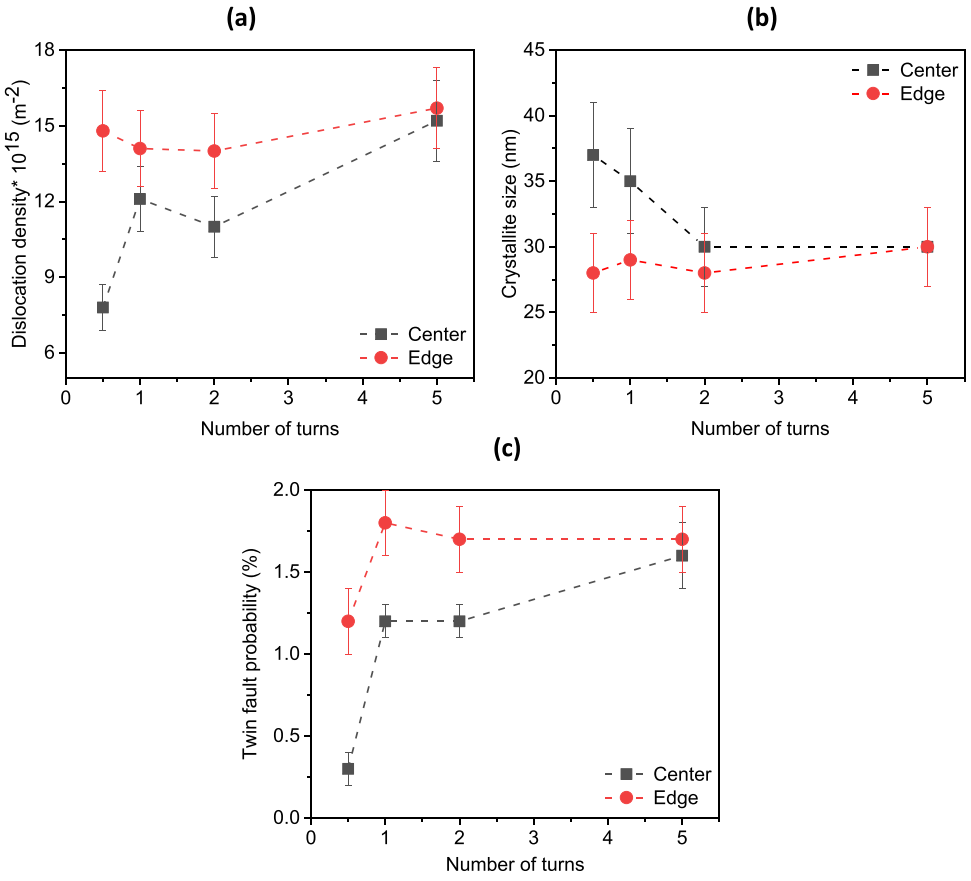

Fig. 6. Variation of (a) dislocation density (b) area-weighted mean crystallite size and (c) twin fault probability as a function of the number of turns by HPT processing as well as the examined location in the disc.

Table 2
Summary of the microstructural parameters obtained by CMWP analysis.

HPT turn/ Location	Crystallite size ($<x>_{area}$) [nm]	Dislocation density (ρ) [10^{14} m^{-2}]	Twin fault probability (β) [%]
½ T, center	37 ± 4	78 ± 9	0.3 ± 0.1
½ T, edge	28 ± 3	148 ± 16	1.2 ± 0.2
1 T, center	35 ± 4	121 ± 13	1.2 ± 0.1
1 T, edge	29 ± 3	141 ± 15	1.8 ± 0.2
2 T, center	30 ± 3	110 ± 12	1.2 ± 0.1
2 T, edge	28 ± 3	140 ± 15	1.7 ± 0.2
5 T, center	30 ± 3	152 ± 16	1.6 ± 0.2
5 T, edge	30 ± 3	157 ± 16	1.7 ± 0.2

demonstrating the lamellar structure, where its SAD pattern in Fig. 8(d) shows evidence of an HCP (ε) phase. It is worth recalling that the present XRD pattern showed no evidence of any second phase apart from FCC for the HPT-processed samples. This suggests that the ε phase is present in very small amount which is below the detection limit of XRD even in a very slow scan. The BF TEM micrograph taken at the edge of the disc after HPT for ½ turn is shown in Fig. 8(e). Significant microstructural refinement compared to its center location was observed. A major phase remained FCC which indicates that further FCC-to-HCP transformation was limited at the disc edge. Nevertheless, the onset of nano-structuring is evident by the ring formation in the SAD pattern as shown in Fig. 8(f).

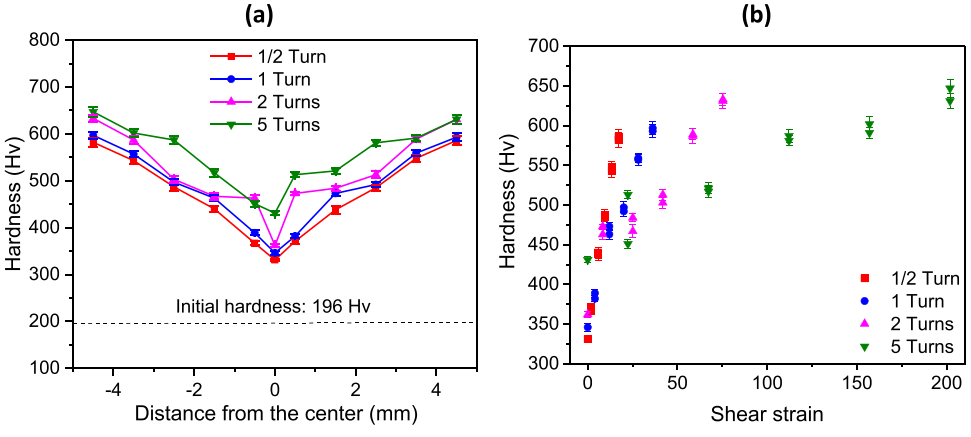

Fig. 7. Variation of micro-hardness as a function of (a) distance from the disc center for different number of turns of HPT processing, and (b) shear strain.

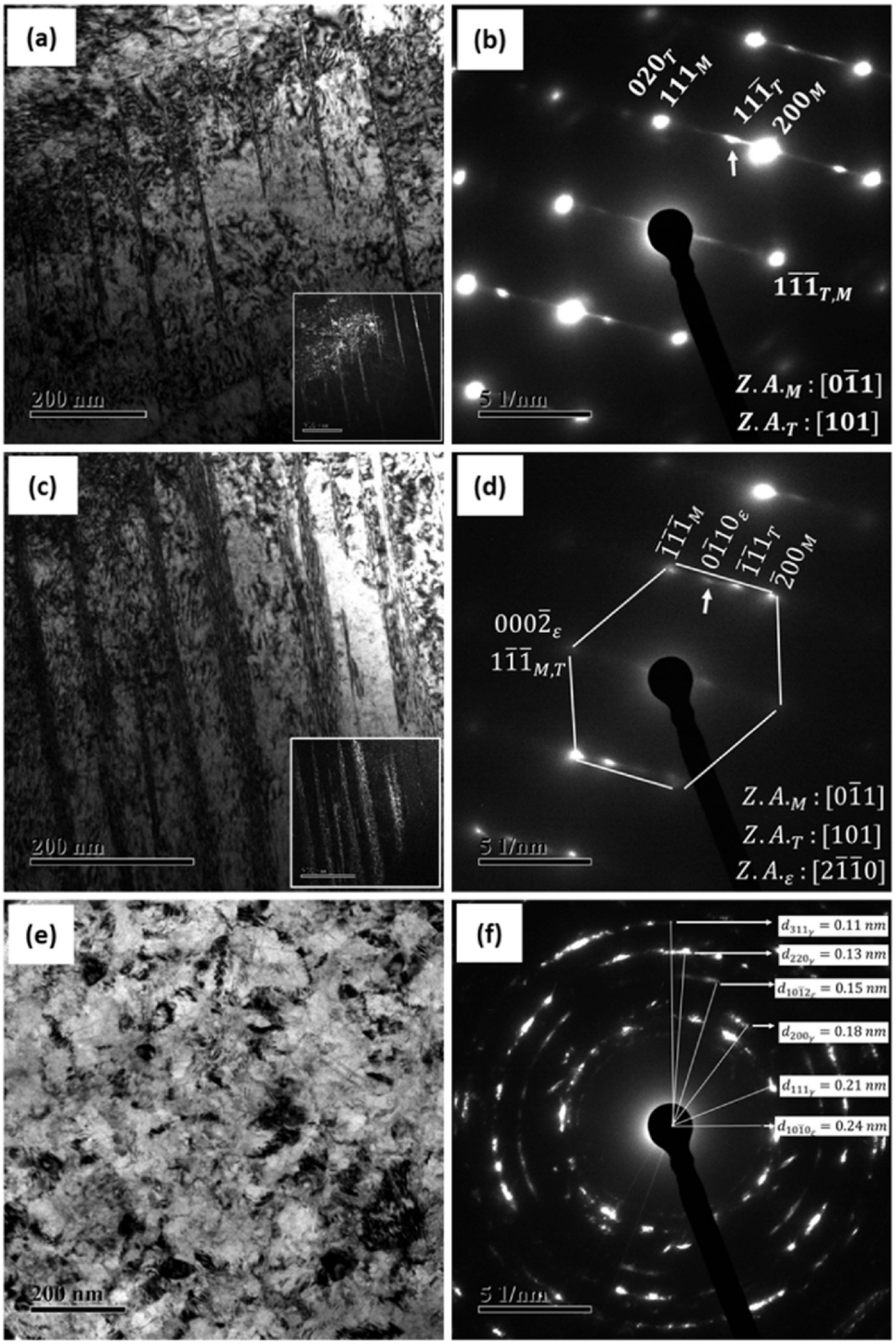

Fig. 8. (a) TEM BF micrograph at the center of the ½ turn HPT-processed specimen (DF micrograph in the inset); (b) corresponding indexed SAD pattern; (c) BF micrograph at another location at the center of the ½ turn HPT-processed specimen (DF micrograph in the inset); (d) corresponding indexed SAD pattern, (e) BF micrograph at the edge of the ½ turn HPT-processed specimen; (g) corresponding indexed SAD pattern.

Fig. 9(a) shows the TEM BF micrograph taken at the center of the 5 turn HPT-processed specimen. Severely deformed structure was observed along with nano-twins with ~5–15 nm spacing. A corresponding SAD pattern in Fig. 8(b) indicates a very limited presence of the ε phase. However, FCC remained as the dominant phase. Nevertheless, nano-structuring at the center after 5 turns is in contrast to the relatively coarser structure at the center of the ½ turn HPT-processed specimen (Fig. 8(a)). A TEM BF micrograph taken at the disc edge after 5 turns is shown in Fig. 9(c) and a corresponding SAD pattern is shown in Fig. 9(d) for revealing the evidence of extensive nano-structuring. Scanning transmission electron microscopy (STEM)-EDS analysis taken at the edge of the nano-structured MEA produced after 5 turns of HPT processing at edge location is shown in Fig. 10. It showed no evidence of precipitation or chemical heterogeneity by demonstrating a homogenous distribution of all the constituent elements.

Fig. 11 shows representative TEM DF micrographs for the samples at (a) ½ turn-center, (b) ½ turn-edge, (c) 5 turns-center and (d) 5

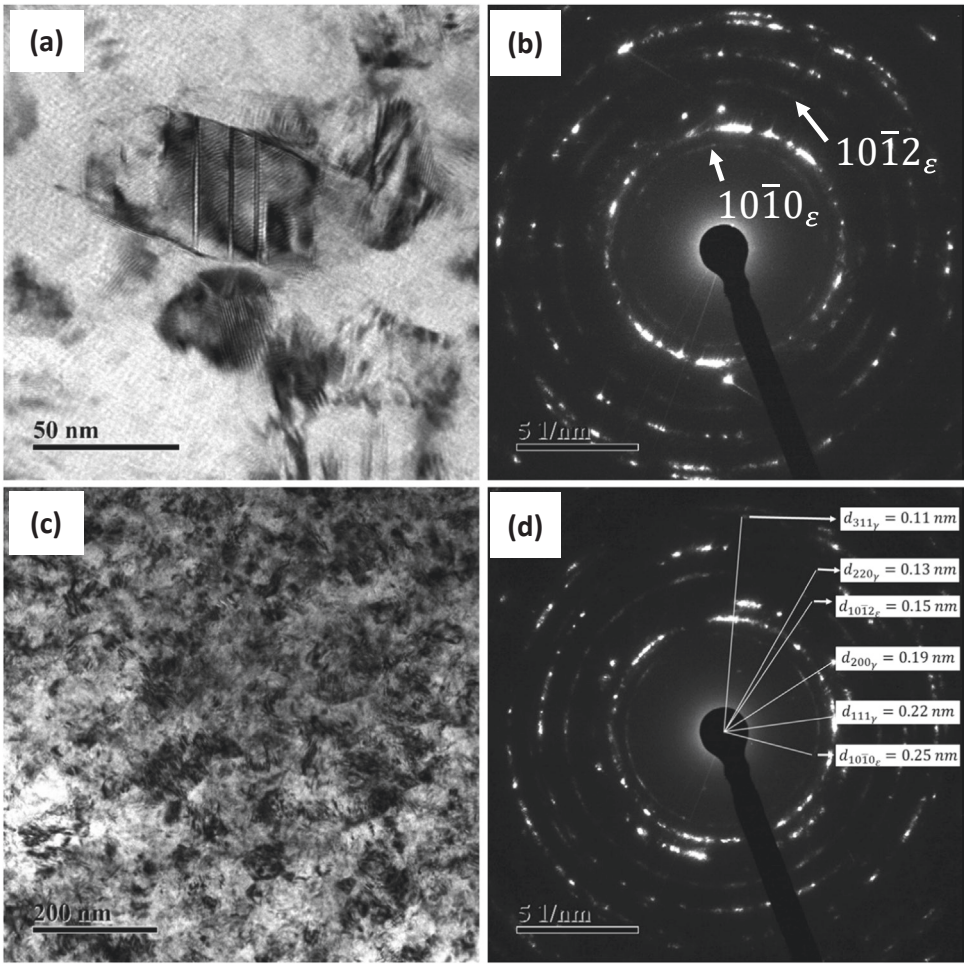

Fig. 9. (a) TEM BF micrograph at the center of the 5 turn HPT processed specimen (b) corresponding indexed SAD pattern; (c) BF micrograph at edge of the 5 turn HPT processed specimen; (d) corresponding indexed SAD pattern.

turns-edge, visualising the evolution of microstructural refinement with HPT processing. The DF images were taken using a (111) type reflection of the FCC phase, with the objective to estimate sequential microstructural refinement. In case of the center in the ½ turn processed specimen, no evidence of nano-structuring was observed. In contrast, under the same HPT-processing condition, there was definitive evidence of nano-structuring near the edge as shown in Fig. 11 (b). In order to quantitatively determine the extent of microstructural refinement, average grain size was measured directly from the DF micrographs for at least 100 grains at a given HPT-processing condition and a specimen location. Nano-structuring was on-going at the edge location of the ½ turn processed specimen, so that a grain size in some regions is as high as ~120 nm and an average grain size was ~76 nm. Clearly, a significant difference in the extent of microstructural refinement was observed between the center and the edge after ½ turn. Likewise, a prominent difference in the extent of microstructural refinement was observed at the center and edge even after 5 turns of HPT processing. Specifically, an average grain size was ~92 nm at the disc center, while it was ~35 nm at the edge of the 5 turn HPT-processed disc. This suggests an absence of the saturation stage in grain refinement despite nearly equivalent dislocation density at these locations for 5 turns. Microstructural refinement to the tune of 30–60 nm grain sizes has also been reported in certain FCC metals and alloys, especially those having medium-to-low SFE [40,49,53].

3.6. Texture evolution during HPT processing

Texture evolution during HPT processing of FCC alloys depends upon the initial texture, grain size and stacking fault energy, and the evolved texture signifies the occurrence of various deformation mechanisms, such as slip, twinning or TRIP. HPT is believed to involve simple shear mode of deformation [54,55], although there may be some deviation owing to quasi-constrained nature of the process and due to application of large compressive force. A monoclinic sample symmetry is used in this study. The predominant simple shear slip systems and their notations are shown in Table 3 [46,56].

The idealized simple shear texture components are provided in Figs. 12 and 13 for the disc centres and edges, respectively, where the measured orientation distribution function (ODF) sections are shown at $\phi_2 = 0°$ and 45°. Although texture evolution during HPT for some other FCC alloys have been described using pole figures, analysis using ODF offers a distinct advantage of the ideal shear components in orientation space without overlap. It is worth noting that the ODF sections presented in Figs. 12 and 13 may not be sufficient to quantify the actual volume fraction of shear texture components since a particular ODF section may not map the overall volume portion of a given texture component. To precisely understand the evolution of different shear texture components, the volume fractions of the shear texture components before HPT and after different numbers of HPT turns is summarized in Table 4. Euler angles of the

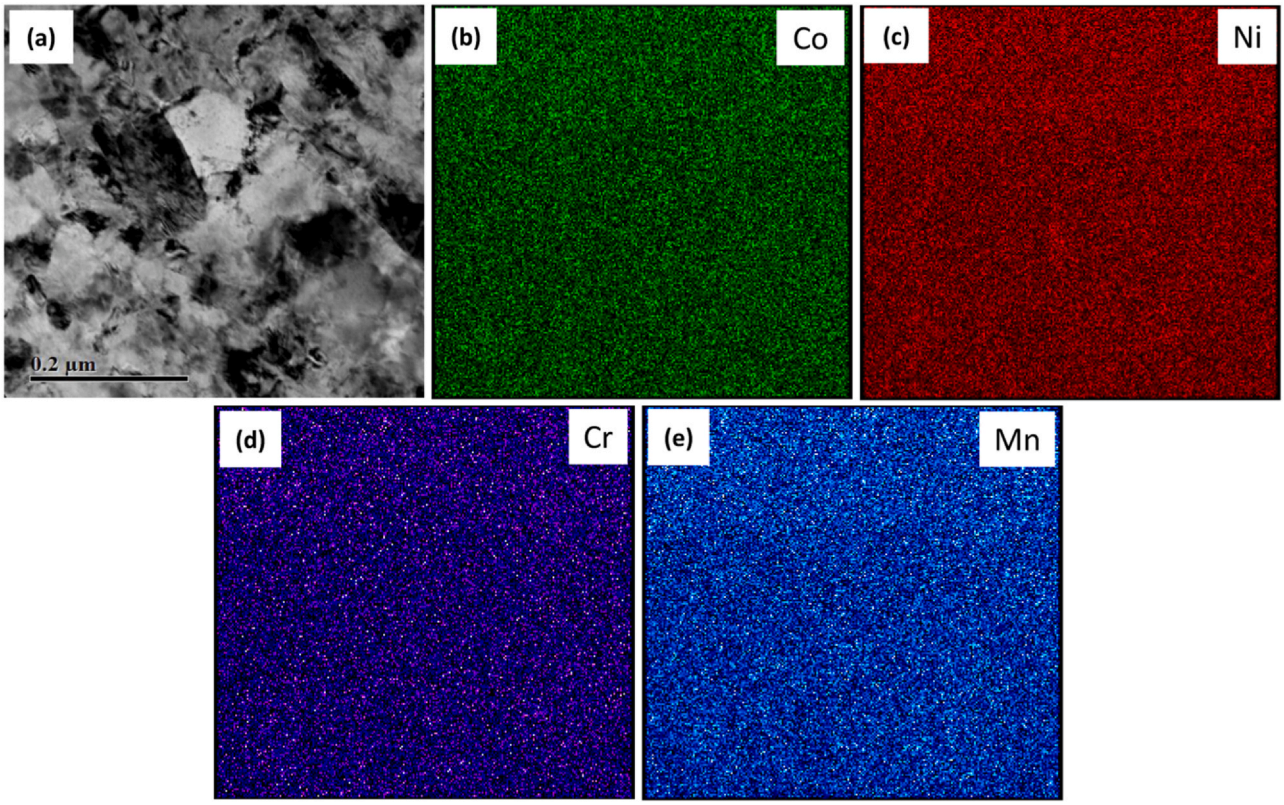

Fig. 10. STEM micrograph and elemental mapping of nano-structured MEA obtained at the edge of 5 turn HPT-processed specimen.

respective shear texture components with a tolerance angle of 15° were used in MATLAB™ toolbox MTEX to calculate the volume fractions of these components in the entire ODF space.

Prior to HPT processing, the disc sample had homogenous texture at the center and edge as presented in Figs. 12 and 13, respectively. The predominant shear texture components were *C, B* and $\bar{B}$ prior to processing (Table 4). Non-shear texture components were also present. As shown in Fig. 12, a remarkable change in the texture components was observed at the center even after ½ turn. Important shear texture components of $\bar{A}$, A_1^* and A_2^* have all strengthened with their individual volume fractions between 2.8% and 2.9%. However, B and $\bar{B}$ components are relatively weaker. The evolution of ideal shear texture components after ½ turn of HPT processing is consistent with a Cu–Ni–Si alloy processed by HPT [57]. Despite a zero theoretical strain at the disc center, evolution of shear texture corroborates with the extensive dislocation activity as revealed by a very high dislocation density of the order of 10^{15} m^{-2} (Table 2). After 1 turn, there was only slight strengthening of the shear texture componenets except C component (rotated Cube), whose fraction showed a considerable increase at the center from ~2.2% for ½ turn to ~3.2% for 1 turn. Evolution of the shear texture components at the center tends to be saturated at 1 turn, as no further change was observed in the texture components through 2 and 5 turns.

The evolution of texture at the disc edges with increasing numbers of HPT turns is presented in Fig. 13. Unlike the disc centers, texture at the disc edges continued to evolve through 5 turns of HPT processing as evidenced from the ODF sections at $\phi_2 = 0°$ and 45°. Furthermore, at any given turn, the texture components are similar but their intensities and volume fractions differ considerably between the centers and edges. The edge showed prominent shear texture components after ½ turn with marked differences from the unprocessed specimen. All seven shear texture components were stronger at the edge compared to the center. Additionally, the volume fractions of all the components were comparable and in the range of 3.0–3.5%. With increasing numbers of HPT turns to 1, significant changes in the $\bar{B}$ and C texture components were observed at the disc edge. The intensified $\bar{B}$ component indicates greater prevalence of twinning mechanism for deformation. In contrast, the C texture component weakened slightly from 3.2% to 2.87%. The prevalence of the B and $\bar{B}$ texture components corroborate with the activation of twinning as evidenced by relatively high twin fault probability and the formation of nano-twins as confirmed by CMWP and TEM investigations respectively [58]. After 2 turns, the shear texture components A, $\bar{A}$, A_1^* and A_2^* strengthened further, while a slight decrease was shown in the volume fraction of the C component. Increasing numbers of turns to 5 introduced a prominent weakening of the B and $\bar{B}$ components compared to the edge after 2 turn. Other important shear texture components have nearly remained invariant. Weakening of the B and $\bar{B}$ components at the disc edge between 2 and 5 turns can be understood on the basis of extensive grain fragmentation [54–56]. It is also worth mentioning that texture at the center and edge of 5 turn processed specimen have identical nature, albeit having different intensities indicating a tendency towards saturation of dislocation mobility at center and edge after 5 HPT turns.

4. Discussion

HPT processing of the novel $Co_{33}Ni_{33}Cr_{19}Mn_{15}$ (at%) MEA led to significant nano-structuring, accumulation of defects including dislocations and twins (TWIP effect) and minor deformation induced phase transformations (TRIP effect). This study generated several interesting insights on the response during nano-structuring by HPT of this alloy in comparison to a range of FCC metals and alloys, which are discussed below.

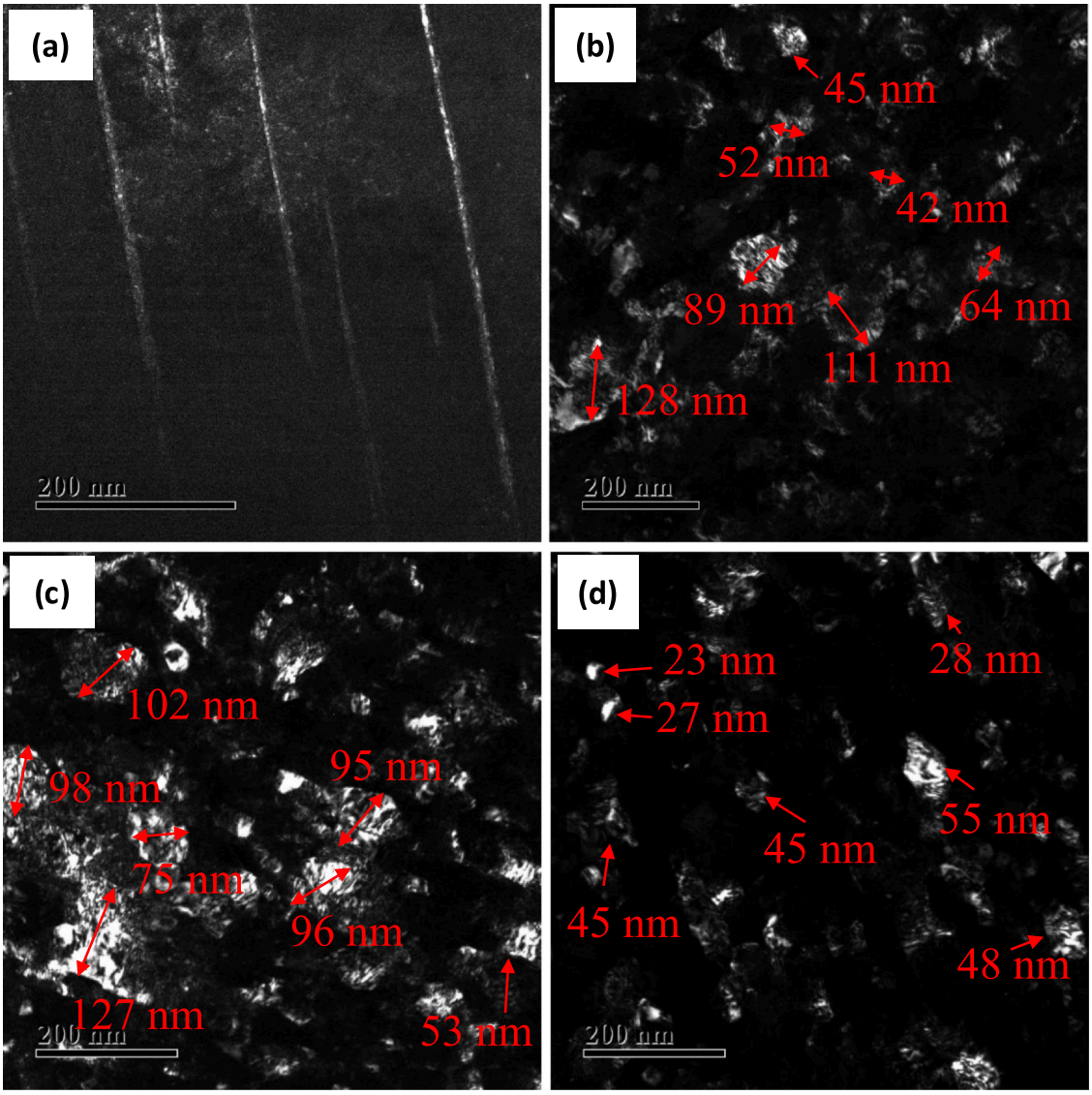

Fig. 11. Representative TEM DF micrographs showing the extent of microstructural refinement: (a) ½ turn- center, (b) ½ turn- edge, (c) 5 turns- center, (d) 5 turns- edge.

Table 3
Ideal simple shear texture components and their Miller indices [46,56].

Texture component nomenclature	Miller indices: {hkl} <uvw>	Euler angles (°)		
		ϕ_1	ϕ	ϕ_2
A	$(11\bar{1})$ $[1\bar{1}0]$	0	35.26	45
$\bar{\boldsymbol{A}}$	$(\bar{1}\bar{1}1)$ $[1\bar{1}0]$	180	35.26	45
$\mathbf{A_1}^*$	$(11\bar{1})$ $[2\bar{1}1]$	35.27	45	0
		125.37	90	45
$\mathbf{A_2}^*$	$(1\bar{1}1)$ $[\bar{2}\bar{1}1]$	144.74	45	0
		54.74	90	45
B	$(11\bar{2})[1\bar{1}0]$	0	54.74	45
		120	54.74	45
$\bar{\boldsymbol{B}}$	$(\bar{1}\bar{1}2)$ $[\bar{1}10]$	60	54.74	45
		180	54.74	45
C	(100) $[0\bar{1}1]$	90	45	0
		0	90	45

4.1. Stability of FCC phase

While FCC HEAs, especially Cantor alloy and its subsets, were believed to have high stability of FCC phase both against temperature and deformation, a number of studies have shown otherwise in the last few years [6,8]. In practice, an occurrence of short-range ordering, clustering and precipitation have been shown to occur during annealing at elevated temperatures, whereas FCC-to-HCP transformation has been reported during deformation of various FCC HEAs [6–10]. In context of HPT processing, a possibility of TRIP effect through FCC-to-HCP transformation is present even in alloys which are otherwise believed to be TWIP HEA [34,35]. Such an anomalous deformation response during HPT may be due to a nearly equal free energies of FCC and HCP phases at room temperature in these alloys [13]. Thus, kinetically constrained nature of FCC-to-HCP transformation which can be overcome by the application of very high pressure [59,60] and very large equivalent strain involved during processing. In the present study, a Mn-added CoCrNi alloy demonstrated FCC as the predominant phase despite being subjected to severe shear strain. In fact, no trace of an HCP phase was detected by the XRD pattern taken near the disc edge through 5 HPT turns leading to γ~200. However, an in-depth TEM investigation showed the presence of an HCP phase at the disc center as early as after ½ turn, where the examined location experiences minimum shear strain among all the processing conditions and investigated locations. Furthermore, the HCP phase was detected in all the HPT-

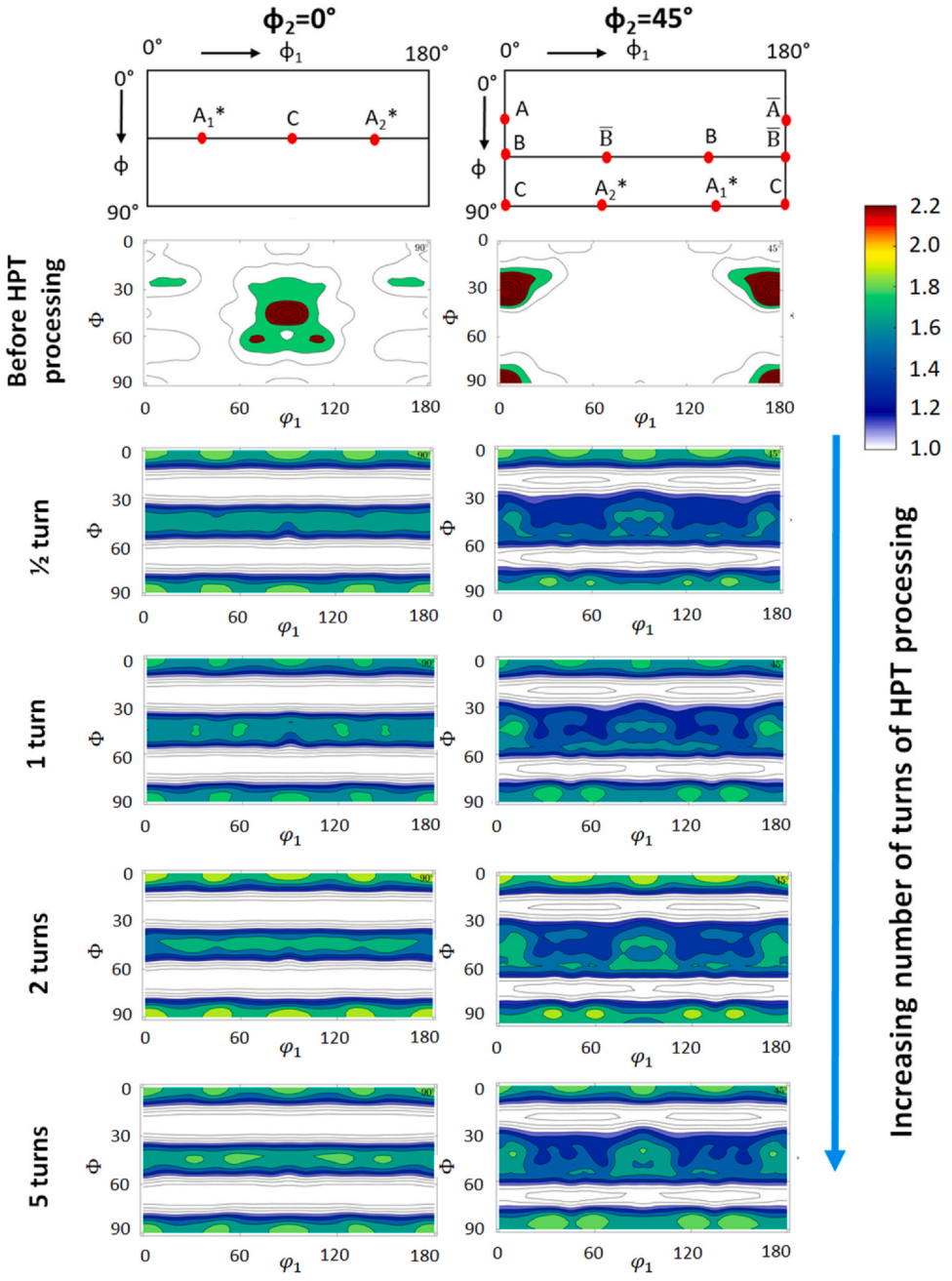

Fig. 12. ODF sections showing the texture evolution at the center of the discs with increasing numbers of turns of HPT processing compared to the ideal simple shear texture components for FCC material at $\phi_2 = 0°$ and 45°.

processed conditions from ½ to 5 turns. However, the fraction of the HCP phase remained quite low and should be less than 5% as it could not be detected using slow-scan XRD. It implies a high resistance to FCC-to-HCP transformation during further HPT processing in the studied alloy. The retardation of continued TRIP effect may be attributed to the following factors:

(i) A rapid increase of dislocation density to the order of 10^{15} m^{-2} at low strains (which was shown at the disc center after ½ turn) that accommodates deformation without phase transformation, leading to an enhanced stability of FCC phase [61].
(ii) Strong grain refinement at high strains resulting in the pronounced grain boundary mediated deformation mechanisms that leads to strain accommodation without the aid of TRIP effect [62,63].

4.2. Stages of evolution of microstructure and hardness

The present alloy exhibited three-stage microstructure evolution with increasing shear strain during HPT processing. For small strains up to ~20 called as Stage I, the dislocation density increased significantly (Table 2), therefore Taylor hardening seems to be the predominant mechanism of strengthening. Additional contributions are expected from TWIP effect introducing nano-twin boundaries (Table 2 and Fig. 8a-b) and minor TRIP effect (Fig. 8c-d) as suggested by the presence of HCP phase. Furthermore, texture with ideal shear components has developed in the disc after ½ turn and might contribute to hardening at this stage. As the strain increases further, there is a subsequent increase in dislocation density to ~10^{16} m^{-2}, which saturated at edge location of ½ turn processed specimen, corresponding to a shear strain of ~20. Here, coarse deformation

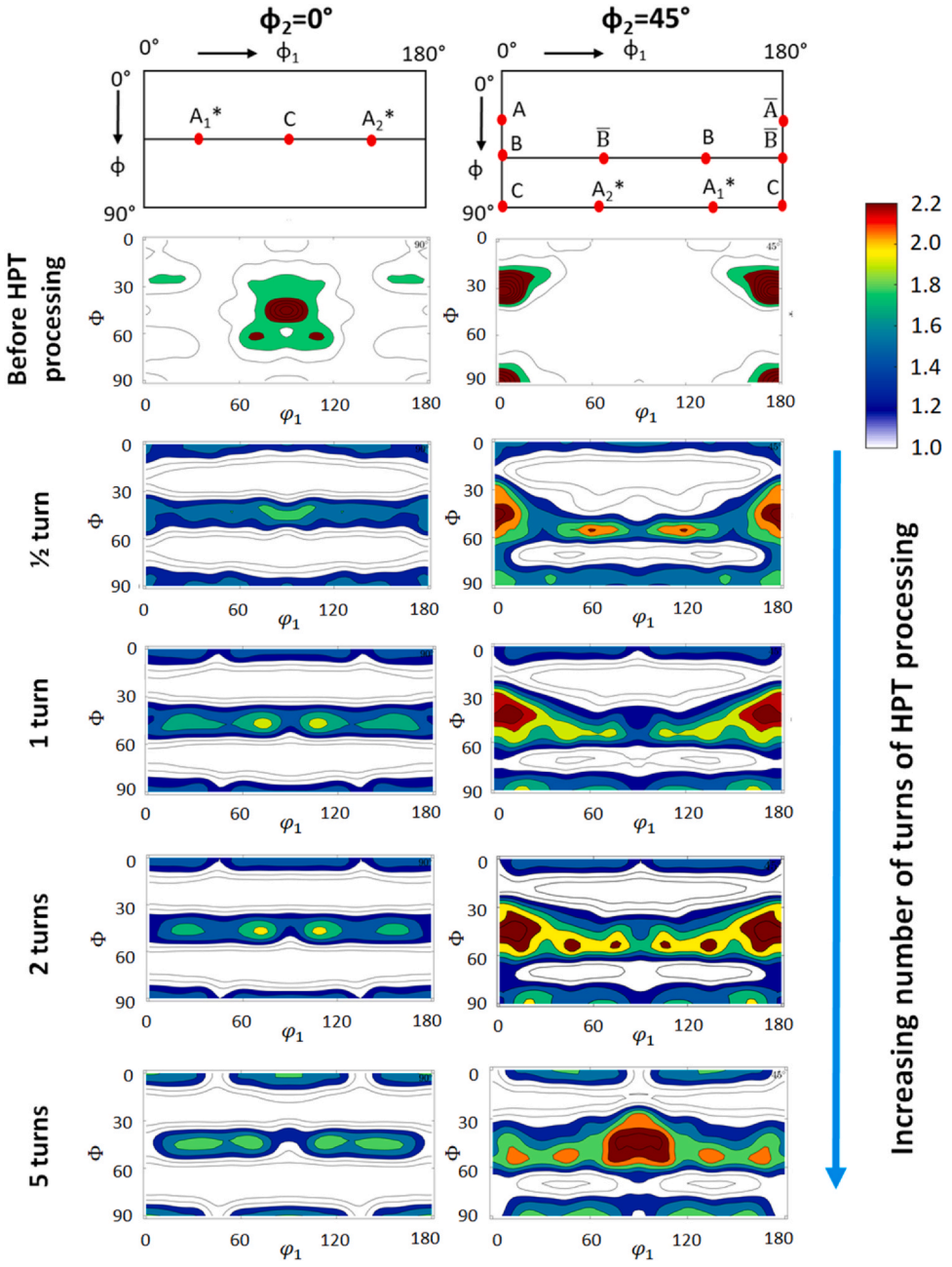

Fig. 13. ODF sections showing the texture evolution at the edge of the discs with increasing numbers of turns of HPT processing compared to the ideal simple shear texture components for FCC material at $\phi_2 = 0°$ and 45°.

Table 4
Volume fractions of different shear texture components at the disc centers and edges with increasing numbers of turns of HPT processing.

No. of turns (Location)	A	$\bar{A}$	A1 *	A2 *	B	$\bar{B}$	C
0 (As received)	0.0183	0.0184	0.0187	0.0191	0.0536	0.036	0.036
0.5 (Center)	0.0289	0.029	0.0288	0.0291	0.0226	0.0224	0.0224
0.5 (Edge)	0.0333	0.0351	0.0351	0.0320	0.0316	0.0307	0.0320
1 (Center)	0.0301	0.0302	0.0297	0.0297	0.0254	0.0246	0.0327
1 (Edge)	0.0345	0.0337	0.0316	0.0364	0.0329	0.0344	0.0287
2 (Center)	0.0308	0.0308	0.0313	0.0308	0.0257	0.0238	0.0332
2 (Edge)	0.0384	0.0369	0.0355	0.0390	0.0309	0.0338	0.0257
5 (Center)	0.0310	0.0307	0.0313	0.0305	0.0257	0.0233	0.0323
5 (Edge)	0.0378	0.0355	0.0393	0.0349	0.0211	0.0208	0.0249

bands with the spacing of ~110–180 nm was observed and there was no evidence of the onset of nano-structuring. In this stage, these microstructural changes yielded a steep increase in hardness as shown in Fig. 7(b). Subsequently, greater than 2.25 times increase in hardness from ~194 Hv to ~450 Hv was observed in this alloy.

After stage I, there is a decrease in a rate of a hardness increase with increasing shear strain, thereby suggesting a drop in a rate of hardening, where it is referred as stage II. The reduced rate of hardening may be attributed to the fact that, dislocation density reached a saturation state at the end of stage I and thereafter Taylor hardening which is a major strengthening mechanism during HPT processing has weakened at stage II. Despite a saturation of dislocation density, an increase in hardness at this stage can be attributed to higher propensity of twinning as indicated by twin fault probability and grain refinement to enter into the domain of nano-structuring. Furthermore, strengthening due to intensification of texture components may also be a contributing factor. This type of microstructure evolution is valid between γ=20–75. Accordingly, hardness increased from ~450 Hv to ~575 Hv in the present MEA.

At stage III of microstructure evolution where γ=75 to ~200, apart from saturation of dislocation density and the TRIP effect, the extent of TWIP effect has also reached a saturation stage. The predominant strengthening mechanism at this stage is grain refinement as is evident from grain size down to ~35 nm at the disc edge after 5 turn. Similar observation of strengthening by grain refinement at later stages of HPT deformation have been reported in an earlier work on a CoCrFeMnNi HEA [64]. In stage III, further decrease in hardening rate was observed, and despite the application of very high shear strain, relatively small hardness increase from ~575 Hv to ~650 Hv was observed.

In terms of processing and location-dependent microstructure evolution, it is worth noting that as shear strain increases with both the number of turns of HPT processing and distance from the center of the disc, hardness also showed a similar relationship. A continued rise in hardness with increasing numbers of turns at the centers of the discs, which is expected to experience zero shear strain, is rationalized based on: (1) a strain gradient model discussed by Estrin et al. which indicates that the gradient in strain progressively decreases from center to periphery of the discs with an increasing number of HPT turns [50], (2) quasi-constrained nature of the process, (3) a continuity of material owing to rotation of neighbouring grains by shear strain introduced at the disc center, (4) small die misalignments, which are inevitable [51,52], and (5) overlapped data recording not only from the center but from its vicinity as well.

The present work presented a systematic investigation of crytallographic texture evolution at the centers and edges of the HPT discs processed through various numbers of turns. Interestingly, even at the center of ½ turn processed disc, initial texture componenets were weakened and were replaced by ideal shear texture components including A, $\bar{A}$, A_1^* and A_2^*. In this study, at any given number of turns, overall shear texture components at edges were stronger than that at the centers due to higher accumulated shear strain at the edges at any given number of turns. Furthermore, prominence of B and $\bar{B}$ texture components is consistent with the proliferation of twinning as evidenced by both TEM and XLPA. In general, shear texture components did not intensify significantly with increasing strain, and such behaviour can be attributed to continued grain fragmentation and nano-structuring [54,56].

4.3. Comparison of hardness evolution during HPT-processing with other FCC materials

Efficacy of HPT processing for a material is primarily determined based on the extent of grain refinement and the achieved hardness compared to the unprocessed condition. The studied MEA having fully FCC structure before HPT processing demonstrated a superior hardness and hardening ability compared to some well-known FCC metals, conventional FCC alloys as well as a recent class of compositionally complex FCC alloys when processing by HPT. Table 5 presents the HPT responses of important FCC materials during HPT processing, underlying deformation mechanisms, peak hardness and hardness ratio (peak hardness / initial hardness of the alloy). Starting with a pure metal such as a high purity Al, HPT processing led to strain-softening and an inverse-Hall-Petch relationship even in a micron-sized grain structure due to the absence of any solute drag effect and grain boundaries acting as dislocation sink [65]. Similar observations of strain-softening during HPT is reported in some other alloys as well [66,67]. With decreasing the purity, HPT-induced hardening has been reported in Al alloys where solute atoms prevented easy cross-slip and climb of dislocations [65]. In contrast to the highly pure Al showing strain-softening during HPT, a pure Ni exhibited significant hardening due to its higher melting point and lower SFE preventing microstructural recovery and thus promoting grain refinement attributing to achieve an average grain size < 175 nm and generating high fractions of low angle grain boundaries and twin boundaries [45,68]. Accordingly, concentrations of Ni and Cu in Cu-Ni alloys have an effect on SFE and homologous temperature, thereby influencing grain refinement during HPT [69]. It should be noted that the grain sizes achieved in the pure Al, Cu, Ni and Cu-Ni alloys could not enter into the domain of true nanocrystalline materials (i.e., their grain sizes were higher than 100 nm). Furthermore, the peak hardness and the hardness ratio were well below than that achieved in the present alloy and other compositionally complex alloys.

The HPT-induced deformation mechanisms and hardness evolution of 316 L stainless steel (SS), in general having common solute elements with many HEAs such as Ni, Co, Cr, Mn in Fe and have medium SFE, appear to be dependent on its manufacturing history. For instance, extensive TRIP effect has been observed for conventionally produced 316 L SS subjected to HPT, whereas twining is the predominant mechanism of deformation during HPT of 316 L SS produced by selective laser melting (SLM) of additive manufacturing [49,70,71]. Moreover, a ratio of the hardness increase by HPT processing for the conventional 316 L SS was significantly greater than for a SLM 316 L SS, and it is due to high initial hardness of SLM 316 L SS having a fine cellular microstructure. However, despite these differences in deformation mechanisms, it resulted in similar peak hardness near periphery of the HPT disc after 5 turns at 6 GPa. The saturated grain size achieved after HPT processing is in the regime of nano-structure for both 316 L SS produced using conventional route and SLM. This may be attributed to its lower SFE compared to Al, Cu, Ni and their alloys. Nonetheless, the peak hardness of 316 L SS was ~600 Hv [49] which is slightly lower compared to the presently studied CoCrNiMn alloy at similar processing condition. This may be explained by the achieved finer grain size in the studied alloy of ~35 nm compared to the 316 L SS showing 55–60 nm. Regarding compositionally complex FCC materials, both HEAs and MEAs displayed the ability to produce a nano-sized grain structure. The reported hardness values of equiatomic CoCrFeMnNi Cantor HEAs after HPT-processing lie in a range of 450–540 Hv [39,64]. This is below the values obtained at the edges of the present alloy. Despite a similar order of magnitude of dislocation density, nano-structured grain size and activation of twinning mechanism, apparently higher hardness achieved in the present alloy may be due to the additional contribution from the initial FCC-to-HCP transformation, which is absent in the Cantor alloy. The present alloy is closer to CoCrNi MEA, which has a higher friction stress and shear modulus (~87 GPa compared to ~80 GPa for Cantor alloy), and it may also lead to additional strengthening, considering the Taylor formula [40]. Likewise, comparing with $Fe_{25}Ni_{25}Co_{25}Cu_{25}$ and $Co_{25}Cr_{25}Fe_{25}Ni_{25}$ HEAs [37,53], the hardness and nano-structuring achieved by HPT processing is significantly superior in the present alloy. Finally, a CoCrNi

Table 5
Comparison of hardness, hardness ratio, deformation mechanisms, grain size and dislocation density in FCC metals and alloys with the present study.

Alloy	Initial hardness (Hv)	HPT Processing condition	Peak hardness (Hv)	Hardness ratio	Deformation mechanism (s)	Grain size after HPT	Dislocation density	Ref.
99.9999% pure Al	18.5 Hv	1 GPa pressure and 15 turns	16.3	0.88	Indication of dynamic recovery and recrystallization	20 μm	–	[65]
A1100 (99% pure Al)	28.4 Hv	6 GPa pressure and 15 turns	87.4	3.07	Impurity atoms prevented easy cross-slip and recovery leading to enhanced hardness	0.4 μm	–	[65]
Pure Ni	~140 Hv	6 GPa and 5 turns of rotation	~350	2.5	Homogeneous microstructure at higher pressure and shear strain with larger fraction of low-angle, twin and special boundaries	~170 nm	–	[45,68]
Pure Ni	–	6 GPa and 5 turns of rotation	~390	–	–	145 nm	–	[69]
Cu			~180			280 nm		
Cu-10 Ni			~ 250			250 nm		
Ni-34Cu			~365			155 nm		
Ni-10 Cu			~370			150 nm		
SLM 316 L stainless steel	~220 Hv	6 GPa and 5 turns of rotation	~560	2.54	Dislocation generation and multiplication, primary and secondary twinning and grain refinement	60 nm	$1.5 * 10^{15}$ m^{-2}	[70]
SLM 316 L SS	233 Hv	6 GPa, 8 turns of rotation	~500	2.14	Predominantly dislocation glide and twinning with small contribution of FCC-to-HCP transformation	60 nm	–	[71]
Conventional 316 L SS	~150 Hv	6 GPa, 5 turns	~550	3.66	Predominant FCC—BCC—HCP transformation	~55 nm	$\sim 1 * 10^{16}$ m^{-2} in martensite phase	[49]
Conventional 316 L SS	150 Hv	6 GPa, 10 turns	~600	4		~45 nm	$\sim 1.3 * 10^{16}$ m^{-2} in martensite phase	
CoCrFeMnNi	122 Hv	6 GPa, 5 turns	~450	3.69	No deformation induced phase transformation	~10 nm	–	[39]
CoCrFeMnNi	~140 Hv	6 GPa, 2 turns	~540	3.85	Extensive twinning	27 ± 5 nm	$1.94 * 10^{16}$ m^{-2}	[64]
$Co_{20}Cr_{26}Fe_{20}Mn_{20}Ni_{14}$	~182 Hv	5 GPa, 5 turns	~510	2.80	Nano-structuring with inadequate recrystallization	61 ± 25 nm	–	[72]
CoCrFeNi	~150 Hv	6 GPa, 20 turns	~500	3.33	Extensive generation and multiplication of dislocations involving twinning suggested by high twin fault probability of ~ 3%	80 ± 10 nm	$\sim 1.5 * 10^{16}$ m^{-2}	[53]
CoCuFeNi	168 Hv	5 GPa, 10 turns	~350	2.08	–	~100 nm FCC phase	–	[37]
CoCrNi	233 Hv	6 GPa, 5 turns	~610	2.62	Nano twins and planar slip	< 50 nm	–	[40]
$Co_{33}Ni_{33}Cr_{19}Mn_{15}$	196 Hv	6 GPa, 5 turns	~650	3.31	Predominantly dislocation slip and twinning with minor FCC-to-HCP transformation in early stage	~35 nm	$\sim 1.6 * 10^{16}$ m^{-2}	Present study

MEA has shown high hardness of ~610 Hv at similar processing conditions [40]. A part replacement of Cr by Mn in this alloy has resulted in: (i) even higher hardness of ~650 Hv, and (ii) a higher ratio of the hardness increase. A higher hardness and hardening ability in the studied $Co_{33}Ni_{33}Cr_{19}Mn_{15}$ alloy compared to the CoCrNi MEA is most likely due to a finer grain size (~35 nm compared to < 50 nm in CoCrNi alloy), and an additional TRIP effect. Additionally, the present alloy showed a very high dislocation density of the order of 10^{16} m^{-2} and high twin fault probability of ~1.7% after HPT-processing, while these are not reported for the CoCrNi alloy.

Accordingly, it is evident that the ability of this novel $Co_{33}Ni_{33}Cr_{19}Mn_{15}$ alloy to concurrently exhibit several strengthening mechanisms of extensive Taylor hardening, nano-structuring, prominent TWIP effect along with minor TRIP effect led to a remarkable combination of peak hardness and hardening ability.

5. Conclusions

This work highlights the sequential microstructure, texture and hardness evolution at the centers and edges of a novel Mn-added $Co_{33}Ni_{33}Cr_{19}Mn_{15}$ FCC medium entropy alloy during HPT processing to different shear strains. Important points from this study are enumerated below:

i) Dislocation slip and twinning were found to be the predominant mechanisms of deformation during HPT processing, whereas FCC-to-HCP phase transformation occurred in a limited amount.
ii) The heterogeneity in the deformation-induced microstructural features was maximum for ½ turn and gradually decreased with increasing number of turns. For 5 turns of HPT processing, the center and edge locations showed similar values for dislocation density, crystallite size and twin fault probability. Despite saturation of these parameters, a marked difference was observed between these examined locations up to 5 turns as confirmed by continuous grain refinement with the measured average grain sizes of ~94 nm at the center and ~35 nm at the edge.
iii) HPT processing resulted in a change in the texture components from strong Goss, Brass and Copper type to simple shear texture even at the disc center after ½ turn. The predominant B and $\bar{B}$ texture components are in line with the activation of twinning. The shear texture components were stronger at the edge compared to center for a given number of turns. A sequential increase in shear strain did not result in proportionate strengthening of shear texture components, which is attributed to extensive nano-structuring involving grain fragmentation.
iv) HPT processing resulted in significant hardening of the alloy (> 3 times higher than the unprocessed alloy). At any given number of turns, hardness at the disc edge was considerably higher than the center which is consistent with the fact that shear strain increases from center to edge. Such higher hardness near the edge than the center in the ½ turn processed specimen may be attributed to increased dislocation density, prominent twinning and the initiation of nano-structuring. In contrast, at higher numbers of turns, continued hardening is predominantly due to significant grain refinement, where other strengthening mechanisms of dislocation density-based Taylor hardening, martensitic transformation, and TWIP effect have saturated much earlier.
v) An addition of Mn to a well-studied equiatomic CoCrNi alloy has resulted in (i) an enhanced hardening ability as reflected by the greater hardness (~650 Hv in $Co_{33}Ni_{33}Cr_{19}Mn_{15}$ alloy vs. ~610 Hv in CoCrNi alloy) and (ii) a higher ratio of the hardness increase by comparing the hardness values before and after HPT (~3.3 in $Co_{33}Ni_{33}Cr_{19}Mn_{15}$ alloy vs. ~2.6 in CoCrNi alloy) under similar HPT processing conditions.

CRediT authorship contribution statement

Kaushal Kishore: Conceptualization, Data curation, Formal analysis, Investigation, Writing – original draft, Visualization, Funding acquisition, Writing – review & editing. **Avanish Kumar Chandan**: Conceptualization, Data curation, Formal analysis, Investigation, Writing – original draft, Visualization, Funding acquisition, Writing – review & editing. **Pham Tran Hung**: Data curation, Investigation. **Saurabh Kumar**: Formal analysis, Investigation; Writing – review & editing. **Megumi Kawasaki**: Formal analysis, Investigation, Writing – original draft, Writing – review & editing. **Jenő Gubicza**: Conceptualization, Supervision, Writing – original draft, Writing – review & editing.

Declaration of Competing Interest

The authors declare that they have no known competing financial interests or personal relationships that could have appeared to influence the work reported in this paper.

Acknowledgements

Fund and a part of equipment support required for carrying out the present study was facilitated by CSIR-National Metallurgical Laboratory, Jamshedpur, India, under the *i*-PSG initiative; Project number: OLP 0346. The study was also supported in part by the National Science Foundation of the United States under Grant No. DMR-1810343.

References

[1] G.K. Bansal, A.K. Chandan, G.K. Mandal, V.C. Srivastava, High entropy alloys: an overview on current developments, in: T.S. Srivastan, M. Gupta (Eds.), High Entropy Alloys: Innovations, Advances, and Applications, CRC Press, Boca Raton, 2020, , https://doi.org/10.1201/9780367374426-1
[2] D.B. Miracle, O.N. Senkov, A critical review of high entropy alloys and related concepts, Acta Mater. 122 (2017) 448–511, https://doi.org/10.1016/j.actamat.2016.08.081
[3] B.S. Murty, J.W. Yeh, S. Ranganathan, P.P. Bhattacharjee, High-Entropy Alloys, Second ed., Elsevier, 2019.
[4] B. Cantor, I.T.H. Chang, P. Knight, A.J.B. Vincent, Microstructural development in equiatomic multicomponent alloys, Mater. Sci. Eng. A 375–377 (2004) 213–218, https://doi.org/10.1016/j.msea.2003.10.257
[5] J.W. Yeh, S.K. Chen, S.J. Lin, J.Y. Gan, T.S. Chin, T.T. Shun, C.H. Tsau, S.Y. Chang, Nanostructured high-entropy alloys with multiple principal elements: novel alloy design concepts and outcomes, Adv. Eng. Mater. 6 (2004) 299–303, https://doi.org/10.1002/adem.200300567
[6] Z. Li, K.G. Pradeep, Y. Deng, Y. Deng, D. Raabe, C.C. Tasan, Metastable high-entropy dual-phase alloys overcome the strength – ductility trade-off, Nature 534 (2016) 227–230, https://doi.org/10.1038/nature17981
[7] B. Schuh, F. Mendez-Martin, B. Völker, E.P. George, H. Clemens, R. Pippan, A. Hohenwarter, Mechanical properties, microstructure and thermal stability of a nanocrystalline CoCrFeMnNi high-entropy alloy after severe plastic deformation, Acta Mater. 96 (2015) 258–268, https://doi.org/10.1016/j.actamat.2015.06.025
[8] F. Otto, A. Dlouhý, K.G. Pradeep, M. Kubenova, D. Raabe, G. Eggeler, E.P. George, Decomposition of the single-phase high-entropy alloy CrMnFeCoNi after prolonged anneals at intermediate temperatures, Acta Mater. 112 (2016) 40–52, https://doi.org/10.1016/j.actamat.2016.04.005
[9] S.A. Kube, J. Schroers, Metastability in high entropy alloys, Scr. Mater. 186 (2020) 392–400, https://doi.org/10.1016/j.scriptamat.2020.05.049
[10] S.S. Nene, P. Agrawal, M. Frank, A. Watts, S. Shukla, C. Morphew, A. Chesetti, J.S. Park, R.S. Mishra, Transformative high entropy alloy conquers the strength-ductility paradigm by massive interface strengthening, Scr. Mater. 203 (2021) 114070, https://doi.org/10.1016/j.scriptamat.2021.114070
[11] N.T. Nguyen, P. Asghari-rad, P. Sathiyamoorthi, A. Zargaran, C.S. Lee, H.S. Kim, Ultrahigh high-strain-rate superplasticity in a nanostructured high-entropy alloy, Nat. Commun. 11 (2020) 2736, https://doi.org/10.1038/s41467-020-16601-1
[12] Y. Tong, D. Chen, B. Han, J. Wang, R. Feng, T. Yang, C. Zhao, Y.L. Zhao, W. Guo, Y. Shimizu, C.T. Liu, P.K. Liaw, K. Inoue, Y. Nagai, A. Hu, J.J. Kai, Outstanding tensile properties of a precipitation-strengthened FeCoNiCrTi 0.2 high-entropy alloy at room and cryogenic temperatures, Acta Mater. 165 (2019) 228–240, https://doi.org/10.1016/j.actamat.2018.11.049
[13] K.G. Pradeep, C.C. Tasan, M.J. Yao, Y. Deng, H. Springer, D. Raabe, Non-equiatomic high entropy alloys: approach towards rapid alloy screening and property-

oriented design, Mater. Sci. Eng. A 648 (2015) 183–192, https://doi.org/10.1016/j.msea.2015.09.010
[14] A.K. Chandan, S. Tripathy, M. Ghosh, S.G. Chowdhury, Evolution of substructure of a non-equiatomic FeMnCrCo high entropy alloy deformed at ambient temperature, Metall. Mater. Trans. A 50 (2019) 5079–5090, https://doi.org/10.1007/s11661-019-05438-z
[15] S.S. Nene, S. Sinha, M. Frank, K. Liu, R.S. Mishra, B.A. McWilliams, K.C. Cho, Unexpected strength-ductility response in an annealed, metastable, high-entropy alloy, Appl. Mater. Today 13 (2018) 198–206, https://doi.org/10.1016/j.apmt.2018.09.002
[16] M. Wang, Y. Lu, T. Wang, C. Zhang, Z. Cao, T. Li, P.K. Liaw, A novel bulk eutectic high-entropy alloy with outstanding as-cast specific yield strengths at elevated temperatures, Scr. Mater. 204 (2021) 114132, https://doi.org/10.1016/j.scriptamat.2021.114132
[17] Y. Lu, X. Gao, L. Jiang, Z. Chen, T. Wang, J. Jie, H. Kang, Y. Zhang, S. Guo, H. Ruan, Y. Zhao, Z. Cao, T. Li, Directly cast bulk eutectic and near-eutectic high entropy alloys with balanced strength and ductility in a wide temperature range, Acta Mater. 124 (2017) 143–150, https://doi.org/10.1016/j.actamat.2016.11.016
[18] M. Wang, H. Cui, Y. Zhao, C. Wang, N. Wei, Y. Zhao, X. Zhang, Q. Song, A simple strategy for fabrication of an FCC-based compositionally complex concentrated alloy coating with hierarchical nanoprecipitates and enhanced mechanical properties, Mater. Des. 180 (2019) 107893, https://doi.org/10.1016/j.matdes.2019 107893.
[19] H.L. Liang, C.W. Tsai, S. Gua, Design of corrosion-resistant high-entropy alloys through valence electron concentration and new PHACOMP, J. Alloy. Compd. 883 (2021) 160787, https://doi.org/10.1016/j.jallcom.2021.160787
[20] Y. Lu, H. Huang, X. Gao, C. Ren, J. Gao, H. Zhang, S. Zheng, Q. Jin, Y. Zhao, C. Lu, T. Wang, T. Li, A promising new class of irradiation tolerant materials: $Ti_2ZrHfV_{0.5}Mo_{0.2}$ high-entropy alloy, J. Mater. Sci. Technol. 35 (2019) 369–373, https://doi.org/10.1016/j.jmst.2018.09.034
[21] R.Z. Valiev, T.G. Langdon, Principles of equal-channel angular pressing as a processing tool for grain refinement, Prog. Mater. Sci. 51 (2006) 881–981, https://doi.org/10.1016/j.pmatsci.2006.02.003
[22] A.P. Zhilyaev, T.G. Langdon, Progress in materials science using high-pressure torsion for metal processing: fundamentals and applications, Prog. Mater. Sci. 53 (2008) 893–979, https://doi.org/10.1016/j.pmatsci.2008.03.002
[23] Y. Saito, N. Tsuji, H. Utsunomiya, T. Sakai, R.G. Hong, Ultra-fine grained bulk aluminium produced by accumulative roll-bonding (ARB) process, Scr. Mater. 39 (1998) 1221–1227, https://doi.org/10.1016/S1359-6462(98)00302-9
[24] Y. Deng, C.C. Tasan, K.G. Pradeep, H. Springer, A. Kostka, D. Raabe, Design of a twinning-induced plasticity high entropy alloy, Acta Mater. 94 (2015) 124–133, https://doi.org/10.1016/j.actamat.2015.04.014
[25] T.W. Zhang, S.G. Ma, D. Zhao, Y.C. Wu, Y. Zhang, Z.H. Wang, J.W. Qiao, Simultaneous enhancement of strength and ductility in a NiCoCrFe high-entropy alloy upon dynamic tension: micromechanism and constitutive modeling, Int. J. Plast. 124 (2020) 226–246, https://doi.org/10.1016/j.ijplas.2019.08.013
[26] G. Laplanche, A. Kostka, C. Reinhart, J. Hunfeld, G. Eggeler, E.P. George, Reasons for the superior mechanical properties of medium-entropy CrCoNi compared to high-entropy CrMnFeCoNi, Acta Mater. 128 (2017) 292–303, https://doi.org/10.1016/j.actamat.2017.02.036
[27] S. Allain, J.P. Chateau, O. Bouaziz, S. Migot, N. Guelton, Correlations between the calculated stacking fault energy and the plasticity mechanisms in Fe-Mn-C alloys, Mater. Sci. Eng. A 387–389 (2004) 158–162, https://doi.org/10.1016/j.msea.2004.01.059
[28] H.T. Jeong, W.J. Kim, Grain size and temperature effect on the tensile behavior and deformation mechanisms of non-equiatomic Fe41Mn25Ni24Co8Cr2 high entropy alloy, J. Mater. Sci. Technol. 42 (2020) 190–202, https://doi.org/10.1016/j.jmst.2019.09.034
[29] W. Li, D. Xie, D. Li, Y. Zhang, Y. Gao, P.K. Liaw, Mechanical behavior of high-entropy alloys, Prog. Mater. Sci. 118 (2021) 100777, https://doi.org/10.1016/j.pmatsci.2021.100777
[30] K. Kishore, R.G. Kumar, A.K. Chandan, Critical assessment of the strain-rate dependent work hardening behaviour of AISI 304 stainless steel, Mater. Sci. Eng. A 803 (2021) 140675, https://doi.org/10.1016/j.msea.2020.140675
[31] P. Sathiyamoorthi, J. Moon, J.W. Bae, P. Asghari-Rad, H.S. Kim, Superior cryogenic tensile properties of ultrafine-grained CoCrNi medium-entropy alloy produced by high-pressure torsion and annealing, Scr. Mater. 163 (2019) 152–156, https://doi.org/10.1016/j.scriptamat.2019.01.016
[32] C.T. Wang, Y. Wang, Microstructural evolution and microhardness variations in a Cu – 36Zn – 2Pb alloy processed by high-pressure torsion Microstructural evolution and microhardness variations in a Cu–36Zn–2Pb alloy processed by high-pressure torsion, J. Mater. Sci. 50 (2015) 1535–1543, https://doi.org/10.1007/s10853-014-8713-2
[33] W. Zhao, J. Han, Y.O. Kuzminova, S.A. Evlashin, A.P. Zhilyaev, A.M. Pesin, J. Jang, K. Liss, M. Kawasaki, Significance of grain refinement on micro-mechanical properties and structures of additively-manufactured CoCrFeNi high-entropy alloy, Mater. Sci. Eng. A 807 (2021) 140898, https://doi.org/10.1016/j.msea.2021.140898
[34] P. Sathiyamoorthi, P. Asghari-rad, G.M. Karthik, Z. Alireza, H.S. Kim, Unusual strain-induced martensite and absence of conventional grain refinement in twinning induced plasticity high-entropy alloy processed by high-pressure torsion, Mater. Sci. Eng. A. 803 (2021) 140570, https://doi.org/10.1016/j.msea.2020.140570
[35] A.K. Chandan, P.T. Hung, K. Kishore, M. Kawasaki, J. Chakraborty, J. Gubicza, Materials characterization on prominent TRIP effect and non-basal slip in a TWIP high entropy alloy during high-pressure torsion processing, Mater. Charact. 178 (2021) 111284, https://doi.org/10.1016/j.matchar.2021.111284
[36] A.K. Chandan, S. Tripathy, B. Sen, M. Ghosh, S.G. Chowdhury, Temperature dependent deformation behavior and stacking fault energy of Fe40Mn40Co10Cr10 alloy, Scr. Mater. 199 (2021) 113891, https://doi.org/10.1016/j.scriptamat.2021.113891
[37] R. Zheng, J. Chen, W. Xiao, C. Ma, Microstructure and tensile properties of nanocrystalline ($FeNiCoCu)_{1-x}Ti_xAl_x$ high entropy alloys processed by high pressure torsion, Intermetallics 74 (2016) 38–45, https://doi.org/10.1016/j.intermet.2016.05.008
[38] P. Edalati, A. Mohammadi, M. Ketabchi, K. Edalati, Microstructure and microhardness of dual-phase high-entropy alloy by high pressure torsion: twins and stacking faults in FCC and dislocations in BCC, J. Alloy. Compd. 984 (2022) 162413, https://doi.org/10.1016/j.jallcom.2021.162413
[39] H. Shahmir, J. He, Z. Lu, M. Kawasaki, T.G. Langdon, Effect of annealing on mechanical properties of a nanocrystalline CoCrFeNiMn high-entropy alloy processed by high-pressure torsion, Mater. Sci. Eng. A 676 (2016) 294–303, https://doi.org/10.1016/j.msea.2016.08.118
[40] S. Praveen, J. Wung, P. Asghari-Rad, J.M. Park, H. Seop, Ultra-high tensile strength nanocrystalline CoCrNi equi-atomic medium entropy alloy processed by high-pressure torsion, Mater. Sci. Eng. A 735 (2018) 394–397, https://doi.org/10.1016/j.msea.2018.08.079
[41] A.K. Chandan, K. Kishore, P.T. Hung, M. Ghosh, S.G. Chowdhury, M. Kawasaki, J. Gubicza, Effect of nickel addition on enhancing nano-structuring and suppressing TRIP effect in $Fe_{40}Mn_{40}Co_{10}Cr_{10}$ high-entropy alloy during high-pressure torsion, Int. J. Plast. (2021) 103193, https://doi.org/10.1016/j.ijplas.2021.103193
[42] A. Saeed-Akbari, J. Imlau, U. Prahl, W. Bleck, Derivation and Variation in Composition-Dependent Stacking Fault Energy Maps Based on Subregular Solution Model in High-Manganese Steels, Metall. Mater. Trans. A 40 (2009) 3076–3090, https://doi.org/10.1007/s11661-009-0050-8
[43] E.G. Astafurova, M.S. Tukeeva, G.G. Maier, E.V. Melnikov, H.J. Maier, Microstructure and mechanical response of single-crystalline high-manganese austenitic steels under high-pressure torsion: The effect of stacking-fault energy, Mater. Sci. Eng. A 604 (2014) 166–175, https://doi.org/10.1016/j.msea.2014.03.029
[44] M. Kawasaki, R.B. Figueiredo, T.G. Langdon, An investigation of hardness homogeneity throughout disks processed by high-pressure torsion, Acta Mater. 59 (2011) 308–316, https://doi.org/10.1016/j.actamat.2010.09.034
[45] A.P. Zhilyaev, G.V. Nurislamova, B.K. Kim, M.D. Baro, J.A. Szpunar, T.G. Langdon, Experimental parameters influencing grain refinement and microstructural evolution during high-pressure torsion, Acta Mater. 51 (2003) 753–765, https://doi.org/10.1016/S1359-6454(02)00466-4
[46] R. Sonkusare, K. Biswas, N. Al-Hamdany, H.G. Brokmeier, R. Kalsar, N. Schell, N.P. Gurao, A critical evaluation of microstructure-texture-mechanical behaviour heterogeneity in high pressure torsion processed CoCuFeMnNi high entropy alloy, Mater. Sci. Eng. A. 782 (2020) 139187, https://doi.org/10.1016/j.msea.2020.139187
[47] G. Ribárik, J. Gubicza, T. Ungár, Correlation between strength and microstructure of ball-milled Al-Mg alloys determined by X-ray diffraction, Mater. Sci. Eng. A. 387–389 (2004) 343–347, https://doi.org/10.1016/j.msea.2004.01.089
[48] M. Soleimani, A. Kalhor, H. Mirzadeh, Transformation-induced plasticity (TRIP) in advanced steels: a review, Mater. Sci. Eng. A 795 (2020) 140023, https://doi.org/10.1016/j.msea.2020.140023
[49] J. Gubicza, M. El-tahawy, Y. Huang, H. Choi, H. Choe, J.L. Lábár, T.G. Langdon, Microstructure, phase composition and hardness evolution in 316L stainless steel processed by high-pressure torsion, Mater. Sci. Eng. A. 657 (2016) 215–223, https://doi.org/10.1016/j.msea.2016.01.057
[50] Y. Estrin, A. Molotnikov, C.H.J. Davies, R. Lapovok, Strain gradient plasticity modelling of high-pressure torsion, J. Mech. Phys. Solids 56 (2008) 1186–1202, https://doi.org/10.1016/j.jmps.2007.10.004
[51] B.Y. Huang, M. Kawasaki, T.G. Langdon, Influence of anvil alignment on shearing patterns in high-pressure torsion, Adv. Eng. Mater. 15 (2013) 747–755, https://doi.org/10.1002/adem.201200363
[52] Y. Huang, A. Al-zubaydi, M. Kawasaki, T.G. Langdon, An overview of flow patterns development on disc lower surfaces when processing by high-pressure, J. Mater. Res Technol. 3 (2014) 303–310, https://doi.org/10.1016/j.jmrt.2014.06.005
[53] J. Gubicza, P.T. Hung, M. Kawasaki, J. Han, Y. Zhao, Y. Xue, J.L. Labar, Influence of severe plastic deformation on the microstructure and hardness of a CoCrFeNi high-entropy alloy: a comparison with CoCrFeNiMn, Mater. Charact. 154 (2019) 304–314, https://doi.org/10.1016/j.matchar.2019.06.015
[54] S. Naghdy, L. Kestens, S. Hertelé, P. Verleysen, Evolution of microstructure and texture in commercial pure aluminum subjected to high pressure torsion processing, Mater. Charact. 120 (2016) 285–294, https://doi.org/10.1016/j.matchar.2016.09.012
[55] B.J. Li, J. Xu, C.T. Wang, D. Shan, B. Guo, T.G. Langdon, Microstructural evolution and micro-compression in high-purity copper processed by high-pressure torsion, Adv. Eng. Mater. 18 (2016) 241–250, https://doi.org/10.1002/adem.201500488
[56] S. Suwas, S. Mondal, Texture evolution in severe plastic deformation processes texture evolution in severe plastic deformation processes, Mater. Trans. 60 (2019) 1457–1471, https://doi.org/10.2320/matertrans.MF201933
[57] A.Y. Khereddine, F.H. Larbi, H. Azzeddine, T. Baudin, F. Brisset, A. Helbert, M. Mathon, M. Kawasaki, D. Bradai, T.G. Langdon, Microstructures and textures of a Cu–Ni–Si alloy processed by high-pressure torsion, J. Alloy. Compd. 574 (2013) 361–367, https://doi.org/10.1016/j.jallcom.2013.05.051

[58] W. Skrotzki, A. Pukenas, B. Joni, E. Odor, T. Ungar, A. Hohenwarter, R. Pippan, E.P. George, Microstructure and texture evolution during severe plastic deformation of CrMnFeCoNi high-entropy alloy, IOP Conf. Series: Materials Science and Engineering 194, 2017. 012028. doi:10.1088/1757–899X/194/1/012028.

[59] C.L. Tracy, S. Park, D.R. Rittman, S.J. Zinkle, H. Bei, M. Lang, R.C. Ewing, W.L. Mao, High pressure synthesis of a hexagonal close-packed phase of the high-entropy alloy CrMnFeCoNi, Nat. Commun. 8 (2017) 1–6, https://doi.org/10.1038/ncomms15634

[60] F. Zhang, Y. Wu, H. Lou, Z. Zeng, V.B. Prakapenka, E. Greenberg, Y. Ren, J. Yan, J.S. Okasinski, X. Liu, Y. Liu, Q. Zeng, Z. Lu, Polymorphism in a high-entropy alloy, Nat. Commun. 8 (2017) 15687, https://doi.org/10.1038/ncomms15687

[61] H.K.D.H. Bhadeshia, R.W.K. Honeycombe, Steels: Microstructure and Properties, fourth ed., Butterworth-Heinemann, 2017.

[62] D. Lee, I. Choi, M. Seok, J. He, Z. Lu, J. Suh, M. Kawasaki, T.G. Langdon, Nanomechanical behavior and structural stability of a nanocrystalline CoCrFeNiMn high-entropy alloy processed by high-pressure torsion, J. Mater. Res. 30 (201) (2015) 2804–2815, https://doi.org/10.1557/jmr.2015.239

[63] M.A. Meyer, A. Mishra, D.J. Benson, Mechanical properties of nanocrystalline material, Prog. Mater. Sci. 51 (2006) 427–556, https://doi.org/10.1016/j.pmatsci.2005.08.003

[64] A. Heczel, M. Kawasaki, J.L. Labar, J. Jang, T.G. Langdon, J. Gubicza, Defect structure and hardness in nanocrystalline CoCrFeMnNi high-entropy alloy processed by high-pressure torsion, J. Alloy. Compd. 711 (2017) 143–154, https://doi.org/10.1016/j.jallcom.2017.03.352

[65] Y. Ito, K. Edalati, Z. Horita, High-pressure torsion of aluminum with ultrahigh purity (99.9999%) and occurrence of inverse hall-petch relationship, Mater. Sci. Eng. A. 679 (2017) 428–434, https://doi.org/10.1016/j.msea.2016.10.066

[66] Y. Huang, J. Millet, N.X. Zhang, P. Jenei, J. Gubicza, T.G. Langdon, An investigation of strain-softening phenomenon in Al – 0.1% Mg alloy during high-pressure torsion processing, Adv. Eng. Mater. 1901578 (2020) 1–7, https://doi.org/10.1002/adem.201901578

[67] M. Kawasaki, Different models of hardness evolution in ultrafine-grained materials processed by high-pressure torsion, J. Mater. Sci. 49 (2014) 18–34, https://doi.org/10.1007/s10853-013-7687-9

[68] A.P. Zhilyaev, S. Lee, G.V. Nurislamova, R.Z. Valiev, T.G. Langdon, Microhardness and microstructure evolution in pure nickel during high-pressure torsion, Scr. Mater. 44 (2001) 2753–2758, https://doi.org/10.1016/S1359-6462(01)00955-1

[69] V.V. Popov, A.V. Stolbovsky, E.N. Popova, Structure of nickel – copper alloys subjected to high-pressure torsion to saturation stage, Phys. Met. Metallogr. 118 (2017) 1073–1080, https://doi.org/10.1134/S0031918×17110114

[70] S.M. Yusuf, Y. Chen, S. Yang, N. Gao, Microstructural evolution and strengthening of selective laser melted 316L stainless steel processed by high-pressure torsion, Mater. Charact. 159 (2020) 110012, https://doi.org/10.1016/j.matchar.2019.110012

[71] J. Han, X. Liu, I. Lee, Y.O. Kuzminova, S.A. Evlashin, K. Liss, M. Kawasaki, Structural evolution during nanostructuring of additive manufactured 316L stainless steel by high-pressure torsion, Mater. Lett. 302 (2021) 130364, https://doi.org/10.1016/j.matlet.2021.130364

[72] J. Moon, Y. Qi, E. Tabachnikova, Y. Estrin, W. Choi, S. Joo, B. Lee, A. Podolskiy, M. Tikhonovsky, H.S. Kim, Microstructure and mechanical properties of high-entropy alloy $Co_{20}Cr_{26}Fe_{20}Mn_{20}Ni_{14}$ processed by high-pressure torsion at 77K and 300K, Sci. Rep. 8 (2018) 11074, https://doi.org/10.1038/s41598-018-29446-y